International Journal of Heat and Mass Transfer 140 (2019) 533–563

Contents lists available at ScienceDirect

International Journal of Heat and Mass Transfer

journal homepage: www.elsevier.com/locate/ijhmt

Flow condensation heat transfer in a smooth tube at different orientations: Experimental results and predictive models

Lucas E. O'Neill [a], R. Balasubramaniam [b,c], Henry K. Nahra [b], Mohammad M. Hasan [b], Issam Mudawar [a,*]

[a] Purdue University Boiling and Two-Phase Flow Laboratory (PU-BTPFL), School of Mechanical Engineering, Purdue University, 585 Purdue Mall, West Lafayette, IN 47907, USA
[b] NASA Glenn Research Center, 21000 Brookpark Road, Cleveland, OH 44135, USA
[c] Department of Mechanical and Aerospace Engineering, Case Western Reserve University, 10900 Euclid Avenue, Cleveland, OH 44106, USA

ARTICLE INFO

Article history:
Received 31 March 2019
Received in revised form 11 May 2019
Accepted 29 May 2019
Available online 13 June 2019

Keywords:
Flow condensation
Heat transfer coefficient
Body force effects
Separated flow model
Correlation evaluation

ABSTRACT

The present study aims to better analyze the influence of body force on flow condensation heat transfer by conducting tests at multiple orientations in Earth's gravity. Dielectric FC-72 is condensed in a smooth stainless-steel tube with 7.12 mm diameter and 574.55 mm condensing length by counterflow of cooling water across the outer surface of the tube. Test conditions span FC-72 mass velocities of 50.3–360.3 kg/m^2 s, test section inlet pressures of 127.0–132.1 kPa, and test section inlet thermodynamic equilibrium qualities of 0.13–1.15. A subset of data gathered corresponding to axisymmetric, annular condensation heat transfer is identified and a detailed methodology for data reduction to calculate heat transfer coefficient presented. Uncertainty analysis is also presented and indicates channel average heat transfer coefficients are calculated within ±3.6% to ±26.7% (depending on operating conditions). Analysis of parametric trends for condensation heat transfer reveals the dominant influence of mass velocity (flow inertia), secondary influence of vapor mass fraction (thermodynamic equilibrium quality), and strong dependence on orientation (body force) at low mass velocities. At higher mass velocities results for all orientations investigated begin to converge, indicating body force independent annular condensation heat transfer is achieved. Separated Flow Model predictions of vertical downflow condensation heat transfer provide reasonable agreement with experimental results, evidence by a Mean Absolute Error (MAE) of 31.2%. Evaluation of condensation heat transfer correlations for horizontal flow reveal most correlations struggle for cases with high liquid content. Specific correlations are identified for superior accuracy in predicting the measured data.

1. Introduction

1.1. Role of flow condensation in phase change thermal management systems

Due to their advantageous coupling of high heat transfer coefficient with high transport capacity, phase change heat transfer processes play important roles in diverse applications including nuclear power generation, HVAC&R, and high flux thermal management [1]. Most work in this field has focused on boiling and evaporation, as precise understanding of heat transfer mechanisms during these processes are required to design cooling systems conforming to specific dimensions of the device(s) being cooled. Although the condensation process is also present within phase change thermal management systems, it has received less attention.

Due to their ability to enhance performance and reduce system footprint, space agencies worldwide are considering implementation of phase change thermal management and energy transport systems. Key targets identified for implementation of these technologies in space include Thermal Control Systems (TCSs), which control temperature and humidity of the operating environment, heat receiver and rejection systems for power generating units, and Fission Power Systems (FPSs), which are projected to provide high power as well as low mass to power ratio [2–4]. Across all prospective applications, a thorough understanding of the influence of body force on both flow boiling and flow condensation heat transfer will be necessary prior to implementation of phase change driven technologies in a microgravity environment.

Many prior studies by researchers at the Purdue University Boiling and Two-Phase Flow Laboratory (PU-BTPFL) and other organizations have investigated both flow condensation and flow

* Corresponding author.
E-mail address: mudawar@ecn.purdue.edu (I. Mudawar).
URL: https://engineering.purdue.edu/BTPFL (I. Mudawar).

https://doi.org/10.1016/j.ijheatmasstransfer.2019.05.103
0017-9310/

Nomenclature

A	area
Bo	Bond number
c_p	specific heat at constant pressure
D	diameter
E	measurement error
f	friction factor
Fr	Froude number
G	mass velocity
g	Earth's gravitational constant
h_{cond}	condensation heat transfer coefficient
h_{fg}	latent heat of vaporization
j	superficial velocity
k	conductivity
K	constant used in calculating eddy momentum diffusivity
L_{cond}	condensation length
$\dot{m}$	mass flowrate
MAE	Mean absolute error
N	number of samples
P	pressure; perimeter
P'	amplitude of pressure fluctuations
P_R	reduced pressure
Pr	Prandtl number
Pwr	power input
Δq_{cond}	local incremental condensation energy transfer
q''	condensation heat flux
Q_{cond}	total condensation energy transfer in test section
Re	Reynolds number
Su	Suratman number
T	temperature
T'	amplitude of temperature fluctuations
t	time
U	uncertainty
u	velocity
v	specific volume
We	Weber number
X_{tt}	Lockhart-Martinelli parameter
x_e	thermodynamic equilibrium quality
y	wall-normal coordinate
z	streamwise position

Greek symbol

δ	condensate film thickness
Γ_{fg}	mass transfer rate per unit length
φ	two-phase multiplier
μ	dynamic viscosity
ρ	density
τ	shear stress
σ	surface tension; standard deviation
θ	test section orientation; percent of predictions within ±30% of experimental value
ζ	percent of predictions within ±50% of experimental value

Subscripts

0-n	indicates a time span ($t = 0$ to $t = n$) over which an average or max is found
ave	average
BH	bulk heater
c	referring to vapor core
f	saturated liquid
F	referring to condensate liquid film
FC	FC-72, condensate
fg	liquid-vapor (commonly for mass transfer due to phase change)
fo	liquid only
g	saturated vapor
go	vapor only
h	hydraulic (diameter)
H2O	water, cooling fluid
i	inner (refers to diameter); interfacial
in	inlet to condensation length (refers to condensate)
max	max value over the range evaluated
mean	mean value over the range evaluated
n	axial measurement station (n = 0–11)
o	outer (refers to diameter)
out	outlet to condensation length (refers to condensate)
sat	saturation
SS	stainless-steel (inner condensation tube)
T	turbulent
Tp	two-phase

Acronyms

CM-HT	condensation module for heat transfer

boiling (commonly employed together) in a variety of configurations. For boiling, these include pool boiling [5,6], flow boiling in macro- [7–12] and micro-channels [13–19], jet impingement [20,21], spray cooling [22–26], and hybrid schemes involving multiple approaches [27]. Condensation configurations include falling film [28–30], flow through single mini-channels [31–38], flow through parallel micro-channel arrays [39–44], and dropwise condensation [45–47]. Although each configuration has unique pros and cons, the present work will focus on flow condensation in smooth, circular tubes, as that is a commonly employed configuration. Most studies in this field share a common deficiency, however, related to understanding of the impact of body force effects on condensation heat transfer.

1.2. Impact of body force effects on flow condensation

Due to the orders of magnitude difference in liquid and vapor phase densities, body force plays a significant role in phase change heat transfer processes. It may act to stabilize or destabilize liquid film motion in vertical flow condensation, drive stratification in horizontal flows, or even act as the driving force in systems operating by natural circulation. Prior studies focusing on the influence of body force on flow condensation have either compared microgravity results to those obtained in 1-g [48] or investigated multiple orientations in 1-g [49].

Some of the earliest works on flow condensation in microgravity were performed by Albers and Macosko [50–52], who investigated nonwetting condensation of mercury during parabolic flights. Results were compared to those obtained from ground testing in horizontal orientation, and show differences depending on operating conditions (i.e., flow quality and mass velocity) investigated.

Similar conclusions were drawn by Keshock [53] who developed an analytic model for flow condensation of R-12 (validated using 1-g data) to investigate potential development of refrigeration systems for application in microgravity. Due to difficulty obtaining microgravity data, however, it was not possible to compare analytic results to corresponding 0-g experiments.

Recently, experimental microgravity data were collected by Lee et al. [54,55] during parabolic flights corresponding to flow condensation of FC-72 in a smooth, 791.12 mm long, 7.12 mm inner diameter tube. An interesting facet of their work is the transition from hyper-gravity through 1-g to microgravity, highlighting the continuously changing flow characteristics dependent on body force intensity.

In 1-g, Wang and Du [56] developed an analytic model and compared results with experimental values obtained for laminar film condensation of steam in inclined tubes. Their model provided reasonable predictive accuracy and validated the key experimental trend of gravity effects decreasing as tube diameter decreases (commonly referred to as confinement effects).

Particularly relevant to the present study are the works of Lips and Meyer, who investigated flow condensation of R-134a in a smooth, 1488-mm long, 8.38-mm inner diameter tube at multiple orientations between −90° (vertical downflow) and +90° (vertical upflow) orientations [57,58]. They provided discussion on influence of body force on parameters including flow regime, heat transfer coefficient, pressure drop, and void fraction, all key design parameters for condensers. In particular, their work noted the strong influence of orientation on condensation pressure drop for cases with low quality (high liquid content), which diminished as quality was increased in the channel.

A concept of gravity-independent flows is seen in the works of Narain and collaborators, who investigated flow condensation of FC-72 experimentally using a smooth, 700-mm long, 6.6-mm inner diameter tube in vertical downflow orientation. They also performed numerical simulations using a 1-D approach, and later 2-D computational (CFD) simulations [59,60]. Although not comparing results from multiple orientations, this work is important as it indicates flow behavior in a single orientation may be dominated by body-force (gravity driven) or interfacial shear effects depending on key operating conditions including mass velocity and flow quality.

O'Neill et al. recently investigated flow condensation of FC-72 in a smooth, 1259.8-mm long, 11.89-mm inner diameter tube in vertical upflow, vertical downflow, and horizontal flow orientations [61,62]. Their work focused on experimental investigation of differences between heat transfer coefficient and liquid film interfacial waves across the three orientations. Conclusions drawn from analysis of experimental results were used to formulate a set of mechanistic criteria, expressed in terms of relevant dimensionless groups, which could be used to determine whether operating conditions could be considered 'gravity-independent' (meaning heat transfer performance would be near-identical for any orientation) or not. Similar to the work of Narain et al. [59,60], flows dominated by body force effects were distinguished from those driven primarily by interfacial shear.

Recent advances in computational capabilities have allowed for full 3-D, unsteady, turbulent flow condensation simulations to be run in multiple orientations. Noori Rahim Abadi et al. recently investigated flow condensation of R134a inside inclined smooth tubes using ANSYS Fluent [63], which complemented earlier experimental work by Lips and Meyer [57,58]. Their conclusion that orientation effects become negligible at high mass velocities (leading to shear-dominated flows) matches well with conclusions from experimental work and helps validate the physicality of computational simulations for flow condensation.

Although the continuing emergence of computational capabilities is expected to eliminate the need for costly experimental payloads in some cases, computational methods for multiphase flows with phase change are not yet at the point where purely predictive results (with no comparison to experimental results under similar operating conditions) may be accepted with high confidence. Because of this, continued experimentation is critical to gain further understanding of how body force affects flow condensation, particularly in the micro-gravity environment. It is here NASA's Flow Boiling and Condensation Experiment (FBCE) aims to obtain unique long-duration microgravity flow condensation data collected onboard the International Space Station (ISS).

1.3. Objectives of study

The present study is part of NASA's Flow Boiling and Condensation Experiment (FBCE), an ongoing collaboration between NASA Glenn Research Center and the Purdue University Boiling and Two-Phase Flow Laboratory (PU-BTPFL) with the goal of developing an experimental facility for the International Space Station (ISS) capable of gathering long term flow boiling and flow condensation data in a microgravity environment. A summary of scientific developments realized as a part of the project can be found in a recent review article by Mudawar [64] (which includes microgravity boiling results [65–67] in addition to condensation).

This work deals with the condensation portion of FBCE and augments prior work dealing with computational prediction of flow condensation [68–70], experimental investigation of flow condensation dynamic behavior [71], and correlation of pressure drop and heat transfer coefficient for condensing flows using a large database from available literature [72,73] with presentation of new heat transfer results.

Key goals for the present work are:

(1) Presentation of a data reduction method for determining flow condensation heat transfer data. This method includes uncertainty analysis and will also be used to process data gathered during the ISS experiments.
(2) Interpretation of key physical trends observable for changes in values of heat transfer coefficient, with special attention paid to the influence of body force.
(3) Evaluation of the Separated Flow Model and commonly used condensation heat transfer coefficient correlations using the new dataset.

In addition, the present work is the companion to another study presenting a new methodology for determination of condensation flow regime in different orientations using only temperature and pressure measurements [74]. Conclusions from the companion work are referenced throughout the current study to provide interpretation of heat transfer trends.

2. Experimental methods

2.1. Condensation module for heat transfer measurements (CM-HT)

Part of NASA's FBCE, the condensation module for heat transfer measurements (CM-HT, shown in Fig. 1(a) and (b)) is a tube-in-tube, counterflow heat exchanger. Condensate (dielectric FC-72) flows through the inner stainless-steel tube possessing inner diameter of 7.12 mm and is condensed along the 574.6-mm condensation length by cooling water flowing through the annulus in the opposite direction. Inlet and exit temperatures and pressures are measured in upstream and downstream (respectively) adiabatic lengths by type-E thermocouples and STS absolute pressure transducers exposed to each respective fluid.

Eleven axial measurement locations are present along the condensation length, with each containing three type-E thermocouples brazed directly to the outer wall of the stainless-steel tube and spaced 120° apart, and two type-E thermocouples inserted into water flowing through the annulus and spaced 180° degrees apart. These axial measurement stations are concentrated near

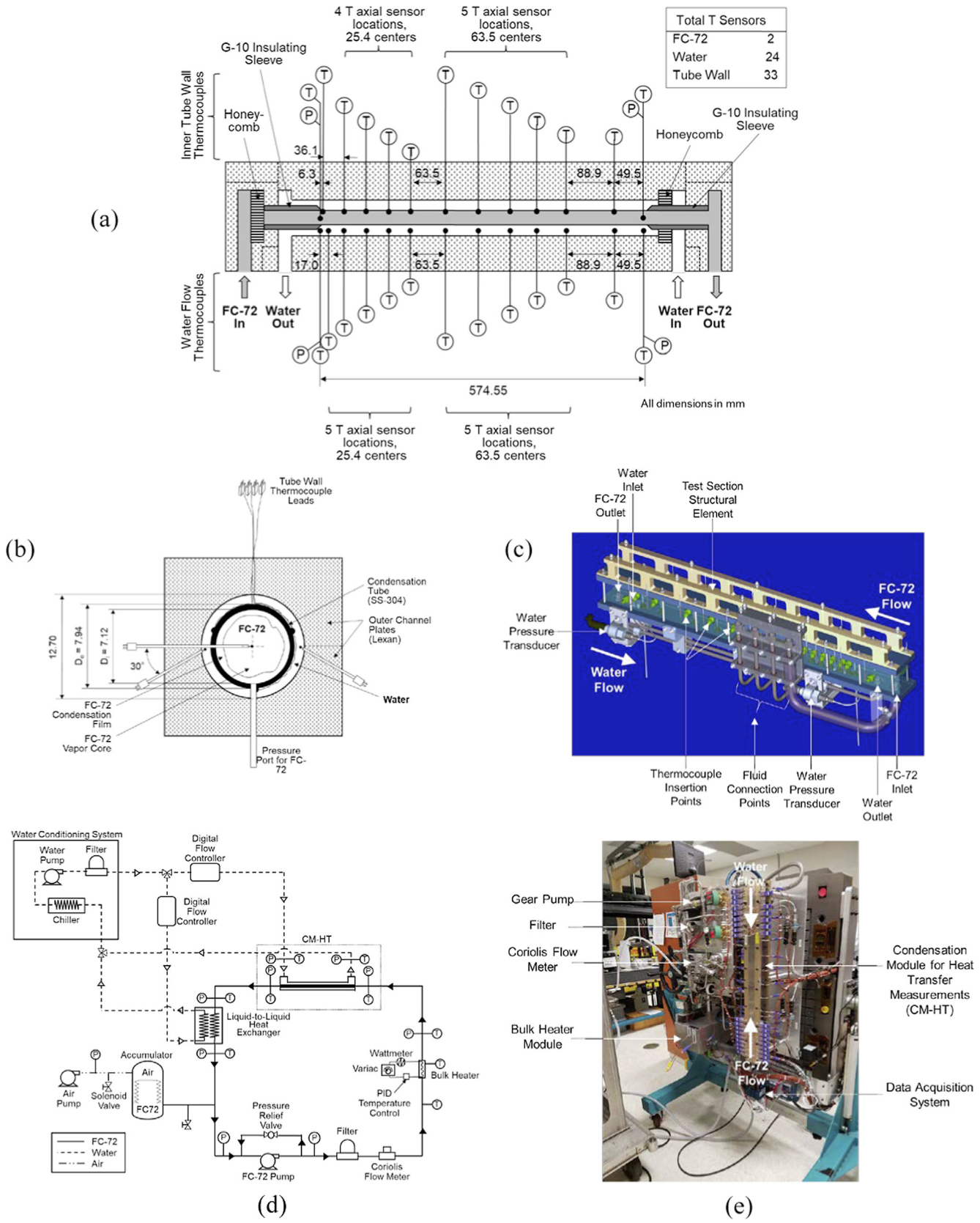

Fig. 1. Condensation Module for Heat Transfer measurements (CM-HT) (a) axial schematic, (b) cross section schematic, and (c) 3-D model, along with (d) schematic and (e) photo of the full experimental facility.

the FC-72 inlet to provide detailed measurements of condensation heat transfer in the upstream region where local behavior changes quickly (with position), with measurement stations near the channel exit spaced further apart as condensate behavior is less dynamic.

Fig. 1(c) provides a 3-D image of the module as it is being designed for the ISS experiment. Key features identified include both water and FC-72 pressure transducers, thermocouple insertion locations, structural elements for mounting within the overall FBCE architecture, and fluid connection points for FC-72 and water. The module used in current experiments was constructed without many of the additional structural elements necessary for the flight payload but maintains the same condensation length characteristics and measurement locations.

2.2. Fluid system

Fig. 1(d) and (e) provide a schematic and photo, respectively, of the fluid system used in the current experiments. Condensate FC-72 is circulated through the primary loop through use of a magnetically coupled Micropump gear pump and passes first through a 5-μm filter to remove any particulates present in the flow. Flow then enters a Coriolis flow meter used to measure flowrate before passing into the bulk heater, used to set thermodynamic conditions at the inlet to the test section.

The bulk heater is configured to reflect the manner it will be utilized in final ISS experiments. Two modes of operation are possible, one with PID control of bulk heater metal temperature and one with constant power provided to the bulk heater. Cases with superheated vapor inlet conditions at the test section inlet are run in temperature-control mode (allowing a constant superheat value to be set at the test section inlet across cases), and those calling for saturated mixture inlet conditions are run in constant-power mode.

Exiting the bulk heater, fluid passes through a short, insulated length prior to reaching the inlet of the test section. Flow through the test section is condensed by cooling water in counter flow configuration, supplied by a secondary water conditioning loop. This loop consists of a Merlin M33 chiller, pump, filter, and Coriolis flow meters along with digital flow controllers for setting and maintaining water flowrate.

After leaving the test section, FC-72 passes through a secondary condenser used to ensure flow is returned to a subcooled liquid state prior to passing the accumulator and returning to the pump. Cooling water for the secondary condenser is also provided by the secondary water conditioning loop. Generally, it may be beneficial to operate these on separate loops (for better control of subcooling on return to the pump), but in an effort to mimic ISS test conditions (where water will be provided to both condensers at identical temperature and pressure) the present setup was used.

2.3. Operating procedure, operating conditions, and measurement uncertainty

Operating conditions for the current tests are a subset of those to be run during the final ISS experiment. Table 1 presents target operating conditions for the current experiments, with every combination of FC-72 mass velocity, operating pressure, inlet quality, and water mass velocity shown in each row tested in vertical upflow, vertical downflow, and horizontal flow orientations. Table 1 indicates a total of 30 tests were run in each orientation, but during the course of experiments this changed slightly based on achievability using the current hardware. Exact operating conditions are provided accompanying results plots throughout the study.

Table 1
Target operating conditions for current study.

G_{FC} [kg/m^2 s]	G_{H2O} [kg/m^2 s]	$P_{FC,in}$ [kPa]	$x_{e,in}$
50	130, 260, 390	130	1.0
100	130, 260, 390	130	1.0
100	390	130	0.4, 0.6, 0.8
150	130, 260, 390	130	1.0
200	130, 260, 390	130	1.0
200	390	130	0.4, 0.6, 0.8
250	130, 260, 390	130	1.0
300	130, 260, 390	130	1.0
300	390	130	0.4, 0.6, 0.8
350	390	130	0.4, 0.6, 0.8

Overall, tests conducted in each orientation amount to 29 cases in vertical upflow and downflow orientations, and 34 cases in horizontal flow orientation, spanning FC-72 mass velocities of G_{FC} = 50.3–360.3 kg/m^2 s, test section water cooling mass velocities *of* G_{H2O} = 129.2–388.4 kg/m^2 s, FC-72 test section inlet pressure of P_{in} = 127.0–132.1 kPa, bulk heater power of Pwr_{BH} = 304.2–1578.1 W, test section inlet thermodynamic equilibrium qualities of $x_{e,in}$ = 0.13–1.15, and test section exit qualities of $x_{e,out}$ = −0.50 to 0.47.

It should be noted here that inlet and exit thermodynamic equilibrium qualities greater than 1.0 and less than 0 refer to superheated and subcooled conditions, respectively. They are calculated according to

$$x_{e,in} = \frac{Pwr_{BH} - \dot{m}_{FC} c_{p,f,FC} \left(T_{FC,sat} - T_{BH,in}\right)}{\dot{m}_{FC} h_{fg,FC}}, \tag{1}$$

and

$$x_{e,out} = \frac{Pwr_{BH} - \dot{m}_{FC} c_{p,f,FC} \left(T_{FC,sat} - T_{BH,in}\right) - \dot{m}_{H2O} c_{p,f,H2O} \left(T_{H2O,out} - T_{H2O,in}\right)}{\dot{m}_{FC} h_{fg,FC}}, \tag{2}$$

where Pwr_{BH}, $\dot{m}$, $c_{p,f}$, and h_{fg} are, respectively, the power supplied to FC-72 by the bulk heater, fluid mass flow rate, liquid specific heat, and enthalpy of vaporization. All fluid properties for each phase are evaluated at local pressures using values provided by NIST. Cases with superheated inlet conditions have inlet quality evaluated directly from measured temperature and pressure. Eq. (1) is only used for cases with saturated mixture inlet conditions and is evaluated after adjusting Pwr_{BH} to account for heat loss.

Test cases were run by first setting FC-72 flow rate, water flow rate, and bulk heater power to levels necessary to achieve the desired inlet conditions. As the system approached steady state tweaks were made to each of these parameters as well as to accumulator gas-side pressure (used to adjust module inlet pressure to the desired value) until the all flow parameters match those desired for the test point. The system was then allowed to sit for 3–5 min to ensure no appreciable deviations from the steady-state operating conditions occurred.

After achieving the desired steady-state operating conditions for the test point, steady-state data was acquired for 2 min at a sampling rate of 200 Hz, then for three minutes at a sampling rate of 5 Hz. Sampling rate was controlled through LabView, with high sampling rate used to facilitate capture of dynamic phenomenon (as was done in a series of recent articles by the present authors [71,74–78]), while also capturing data at a lower sampling rate (5 Hz) matching that to be used on the final ISS experiment. All data presented within the current study was captured at 5 Hz.

Data collection for all temperature, pressure, flow rate, and power measurements is handled by a cDaQ-9178 data acquisition system with one NI-9205 analog input module and four NI-9214 thermocouple modules, all controlled by LabView. Temperature

measurements made with type-E thermocouples have uncertainty of ±0.4 °C, pressure measurements made with STS absolute pressure transducers have uncertainty of ±0.1% of their readings, flow rate measurements (and thus mass velocities) made with Coriolis flow meters have uncertainty of ±0.2% of their readings, and bulk heater power input calculated from voltage and current data has uncertainty of ±0.2 W. After data reduction, this leads to uncertainties for channel average heat transfer coefficient in the range ±3.6% to ±26.7% (depending on operating conditions). Local values of heat transfer coefficient may have higher uncertainties, however, due to the small temperature differences used in their calculation.

Calculation of uncertainty for reported values of condensation heat transfer coefficient is a critical task, and as such is deserving of more thorough presentation. The following section will outline the portion of the dataset used for analysis, methodology employed for calculation of condensation heat transfer coefficient, and will conclude with a detailed presentation of uncertainty propagation for values of condensation heat transfer coefficient.

3. Data selection and heat transfer reduction

Many researchers develop condensation heat transfer models which treat heat transfer mechanisms differently depending on condensation flow regime [80–82]. The necessity of accurately predicting flow regime and understanding its impact on condensation heat transfer behavior is discussed at length in the companion study [74], but key highlights will be discussed here as some context is needed for the decision to choose only a subset of the full database on which to investigate heat transfer behavior.

3.1. Condensation flow regime

Fig. 2 presents schematics of key differences in flow behavior for operating conditions investigated as part of the present study. Two key distinguishing factors are seen for flow condensation depending on orientation and mass flowrate: (1) whether flow is co-current or counter-current (referring to liquid and vapor phases), and (2) whether flow is stratified or annular (referring to liquid film distribution around the channel circumference). The first two rows in Fig. 2, corresponding to vertical upflow condensation with low and high mass flow, respectively, show the key difference in vertical upflow is evident in liquid film motion along the channel. For low mass flow cases, liquid motion can be counter to vapor motion, leading to *falling film*, *flooding*, and *oscillating film* flow regimes, while high mass flow cases yield co-current *annular* flow. Liquid film distribution around the channel circumference is seen to be symmetric for both low and high flowrate cases in vertical upflow orientation.

Fig. 2 shows how vertical downflow condensation is always expected to exhibit axymmetric, co-current *annular* flow for all operating conditions. Interfacial waviness is expected to vary depending on relative magnitudes of flow inertia and body force, but the presence of body force acting parallel to flow direction has a stabilizing effect on liquid film motion relative to other orientations.

Finally, the last two rows of Fig. 2 illustrate the key difference for horizontal flow cases is between axisymmetric and stratified liquid film distribution around the channel circumference. Now acting perpendicular to flow direction, body force no longer impacts liquid film motion along the channel as was seen in upflow and downflow orientations but does drive liquid to accumulate near the bottom of the channel for cases with low flow inertia. This leads to manifestation of *stratified*, *wavy stratified*, and *plug* flow regimes. In high flowrate cases flow inertia is sufficient to support formation of liquid film near the top of the channel, leading to establishment of axisymmetric *annular*, *wavy annular*, and *slug* flow regimes.

As mentioned previously, liquid film distribution and motion within the channel plays a dominant role on heat transfer. Counter-current flow regimes in vertical upflow lead to strong periodicity and increase effects such as liquid film breakup and droplet impingement compared to that seen for co-current flow. In horizontal flow, the presence of stratified flow can significantly decrease heat transfer coefficient due to the greatly increased liquid film thickness near the bottom of the channel and reduced interfacial perimeter (compared to annular flow).

Due to these effects it is important to know what flow regime is expected for a given set of operating conditions and so results can be analyzed with that in mind. The companion study [74] provided a new method for determining condensation flow regime based on temperature and pressure measurements. Key outcomes from that work are presented in Fig. 3.

Fig. 3(a)–(c) deal with distinguishing counter-current and co-current vertical upflow cases. This was done using scaled temperature and pressure fluctuations, defined as

$$\begin{aligned} \textit{scaled temperature fluctuation} &= \frac{T'}{T_{ave}} \times 100\% \\ &= \frac{0.5(\max(T_{0-n}) - \min(T_{0-n}))}{mean(T_{o-n})} \times 100\%, \end{aligned} \tag{3}$$

and

$$\begin{aligned} \textit{scaled pressure fluctuation} &= \frac{P'}{P_{ave}} \times 100\% \\ &= \frac{0.5(\max(P_{0-n}) - \min(P_{0-n}))}{mean(P_{o-n})} \times 100\%, \end{aligned} \tag{4}$$

respectively. In general terms, these parameters are equal to the maximum amplitude of fluctuation observed over some time period $t_0 - t_n$, divided by the average value of the parameter (temperature or pressure) over the same period (in °C and kPa, respectively). The end value is then expressed as a percentage, hence the multiplication by 100. These values are calculated locally then averaged along the channel length to provide a single value for each set of operating conditions shown in Fig. 3. This method of dynamic analysis is based on work by the current authors on characterizing flow boiling oscillatory behavior [75–78], and full details on these calculations are available in the companion study [74].

Fig. 3(a) shows values of scaled temperature fluctuations for vertical upflow with superheated vapor inlet conditions. Values are seen to converge to a near-constant level between FC-72 mass velocities of G_{FC} = 100–150 kg/m^2 s, and remain largely constant thereafter. This indicates the transition from regimes with noticeable periodicity (counter-current flow regimes such as *falling film*, *flooding*, and *oscillating film*) to a regime without these effects (*annular* co-current flow).

Fig. 3(b) illustrates a similar convergence in value for vertical upflow cases with saturated mixture inlet conditions, although this time occurring at a higher mass velocity than for cases with superheated inlet conditions. This is liquid due to increased liquid content within the channel delaying the transition from gravity-dependent to gravity-independent flow regimes.

Fig. 3(c) reinforces the trends observed for scaled temperature fluctuations by presenting results for scaled pressure fluctuations corresponding to both inlet (top) and exit (bottom) pressure measurements. Corresponding results for vertical downflow cases are also present on plots in Fig. 3(c) to show how vertical upflow scaled pressure fluctuations are significantly higher for low flowrate cases, with the difference decreasing as mass velocity is increased until near-identical results are seen for high FC-72 mass velocities. Vertical downflow condensation is known to be *annular*

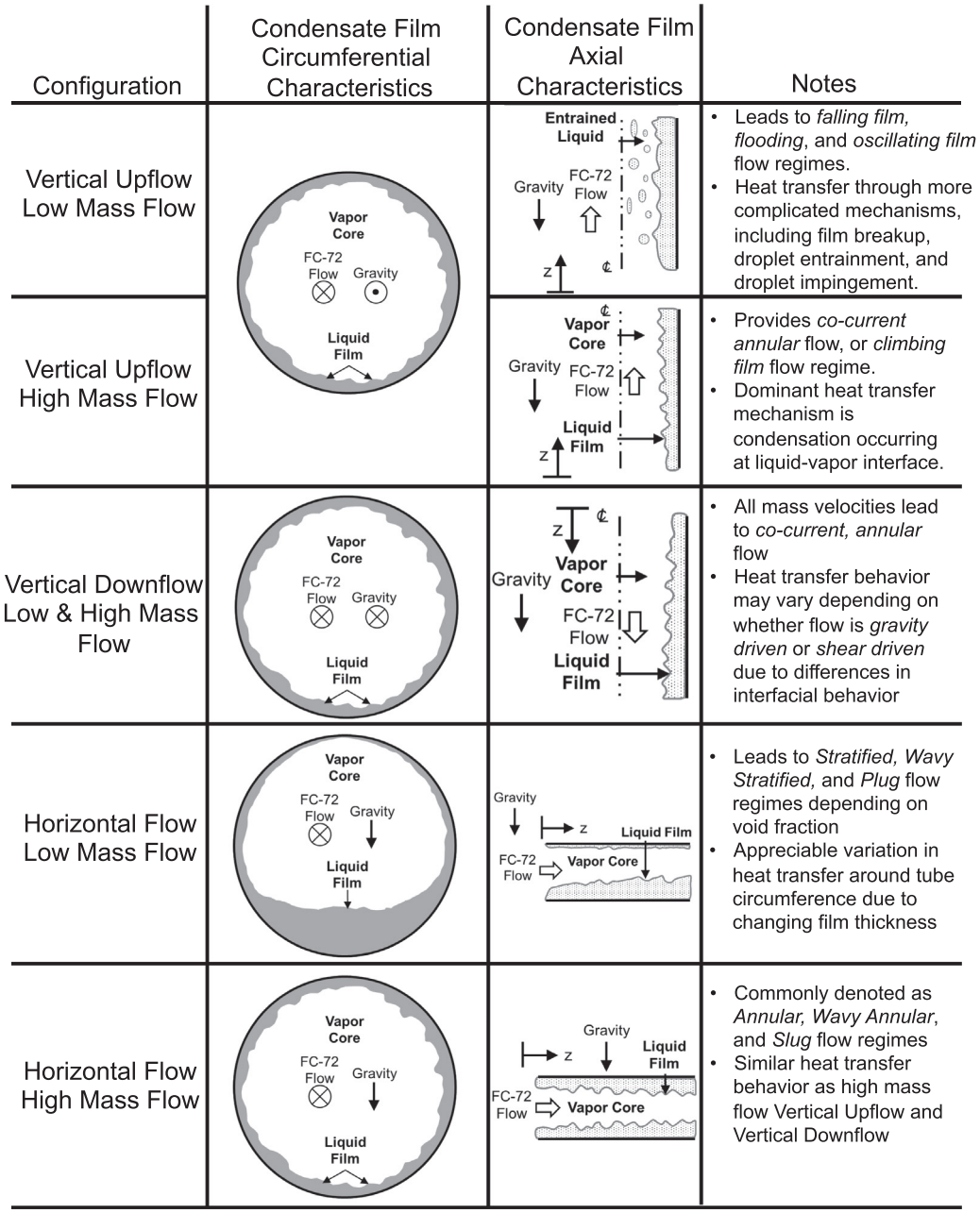

Fig. 2. Key features of condensate liquid film distribution across vertical upflow, vertical downflow, and horizontal flow orientations, along with the impact of each on heat transfer performance.

and co-current for all operating conditions due to the stabilizing influence of gravity, so the convergence of vertical upflow behavior to match that of vertical downflow is a strong indicator *annular*, co-current flow is achieved for high mass velocity vertical upflow cases.

Fig. 3(d) provides similar analysis for distinguishing between stratified and axisymmetric flow cases in horizontal flow, this time using standard deviation of circumferentially spaced stainless-steel temperature measurements. Fig. 1 showed all eleven axial measurement locations along the module's condensation length possess three wall temperature measurements separated by 120°, and by calculating the standard deviation between these and averaging along the channel length it becomes possible to provide a single representative value of circumferential temperature variation for each set of operating conditions. As mentioned for fluctuating temperatures and pressures, full details on calculation of these parameters may be found in the companion study [74], as well as additional information on local temperature measurements.

Fig. 3(d) shows values of channel averaged stainless-steel temperature standard deviations for vertical upflow, vertical downflow, and horizontal flow cases, plotted versus FC-72 mass velocity. At low FC-72 mass velocities horizontal flow exhibits standard deviations 3–4 times larger than those for vertical orientations, indicating the presence of strong temperature gradients along the tube circumference. These temperature gradients are due to the presence of stratified flow leading to significantly lower temperatures along the bottom of the tube (with thick liquid layer separating the tube wall from hot FC-72 vapor) and high temperature along the top wall (exposed to hot FC-72 vapor). As mass velocity increases these differences become less noticeable, with results for $G_{FC} \sim 200$ kg/m^2 s and greater exhibiting nearly identi-

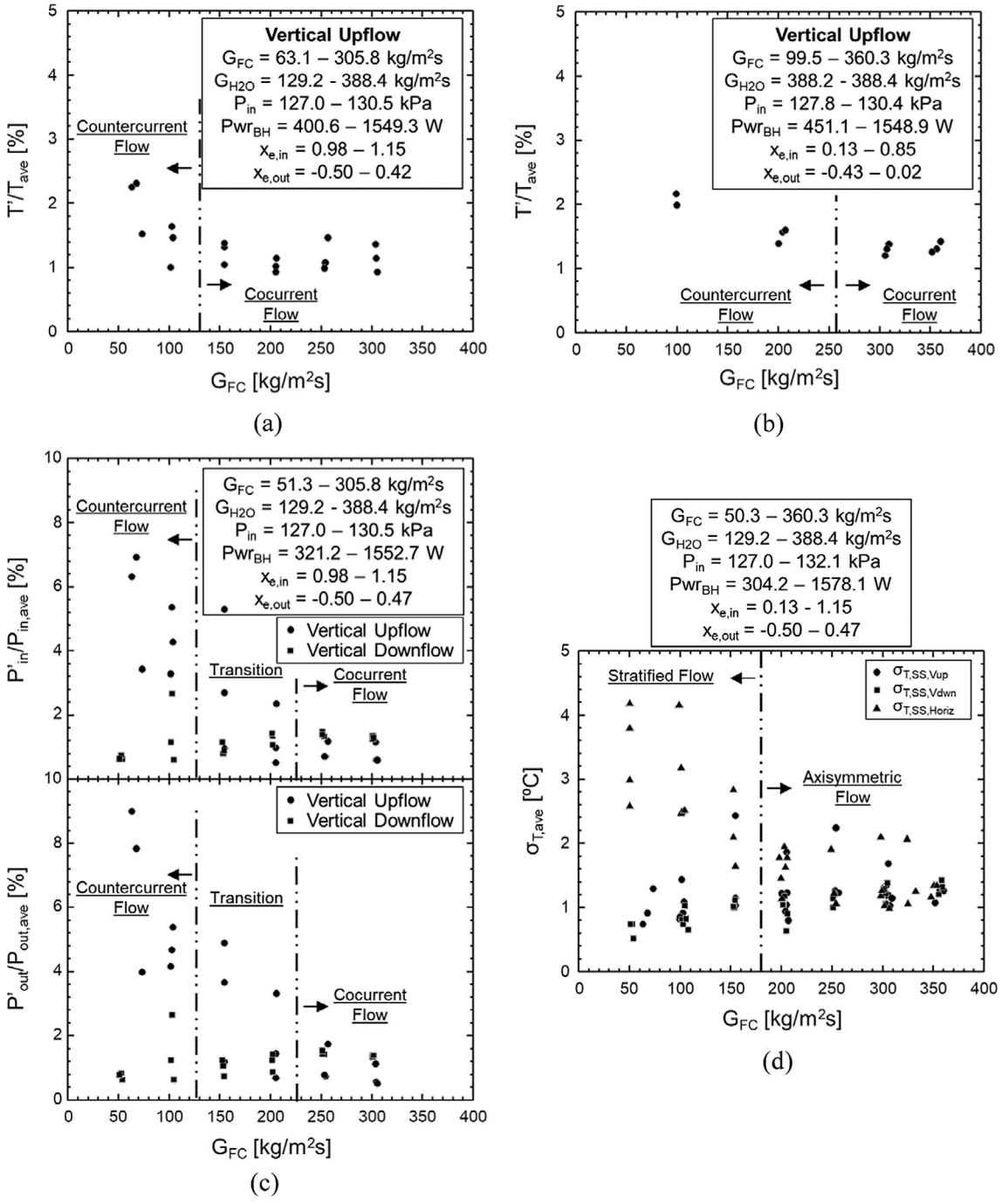

Fig. 3. Results from the companion study to the present work [–] illustrating experimentally observed boundaries between counter-current and co-current flow (referring to liquid and vapor phases in vertical upflow) determined using temperature fluctuations for (a) superheated inlet conditions and (b) saturated mixture inlet conditions, and (c) the same using pressure fluctuations. Stratified and axisymmetric flows in horizontal orientation are distinguished in (d) using standard deviation between circumferentially spaced temperature measurements.

cal results for all three orientations indicating horizontal flow has transitioned to a more axisymmetric flow regime (*annular* or *wavy annular*). Based on this, horizontal flow tests cases presented here are limited to those with $G_{FC} > 200$ kg/m^2 s.

These differences in condensation flow regime will become important in later subsections, as they will be used to limit the scope of heat transfer analysis to focus only on axisymmetric cases, as well as discuss impact of counter-current flow conditions on heat transfer in vertical upflow. Should investigators become interested in detailed study of stratified or other asymmetric condensation regimes, design of condensation test sections to utilize additional circumferentially spaced thermocouples [61,62,79] is recommended.

Prior to discussing heat transfer results, it is necessary to provide a detailed description of the methodology used to calculate condensation heat transfer coefficient for the present set of experimental results.

3.2. Condensation heat transfer coefficient calculation

As mentioned when describing the test section (CM-HT) in Section 2, thermocouples are included at 11 axial locations along the

condensation length for measuring heat transfer. Each measurement location contains three thermocouples brazed to the outer surface of the stainless-steel tube (spaced 120° apart) and two thermocouples inserted into the water flow (spaced 180° apart). The first step in heat transfer data reduction is to average the two water temperatures and three stainless-steel temperatures at each axial location to provide a single representative temperature for water and stainless-steel at all 11 measurement points. As shown in Fig. 4(a), this allows a 1-D, radial energy balance to be performed to calculate condensation heat transfer coefficient (with the assumption of axisymmetric behavior at all axial locations).

It should be noted that significant effort was spent analyzing standard deviation between local measurements conducted at each axial location in the companion study [74], as these values were used to identify the transition from stratified to annular flow for cases in horizontal orientation. Stratified horizontal flow condensation lead to significant differences between stainless-steel temperature measurements at the same axial location (as discussed in the preceding subsection), meaning that taking an

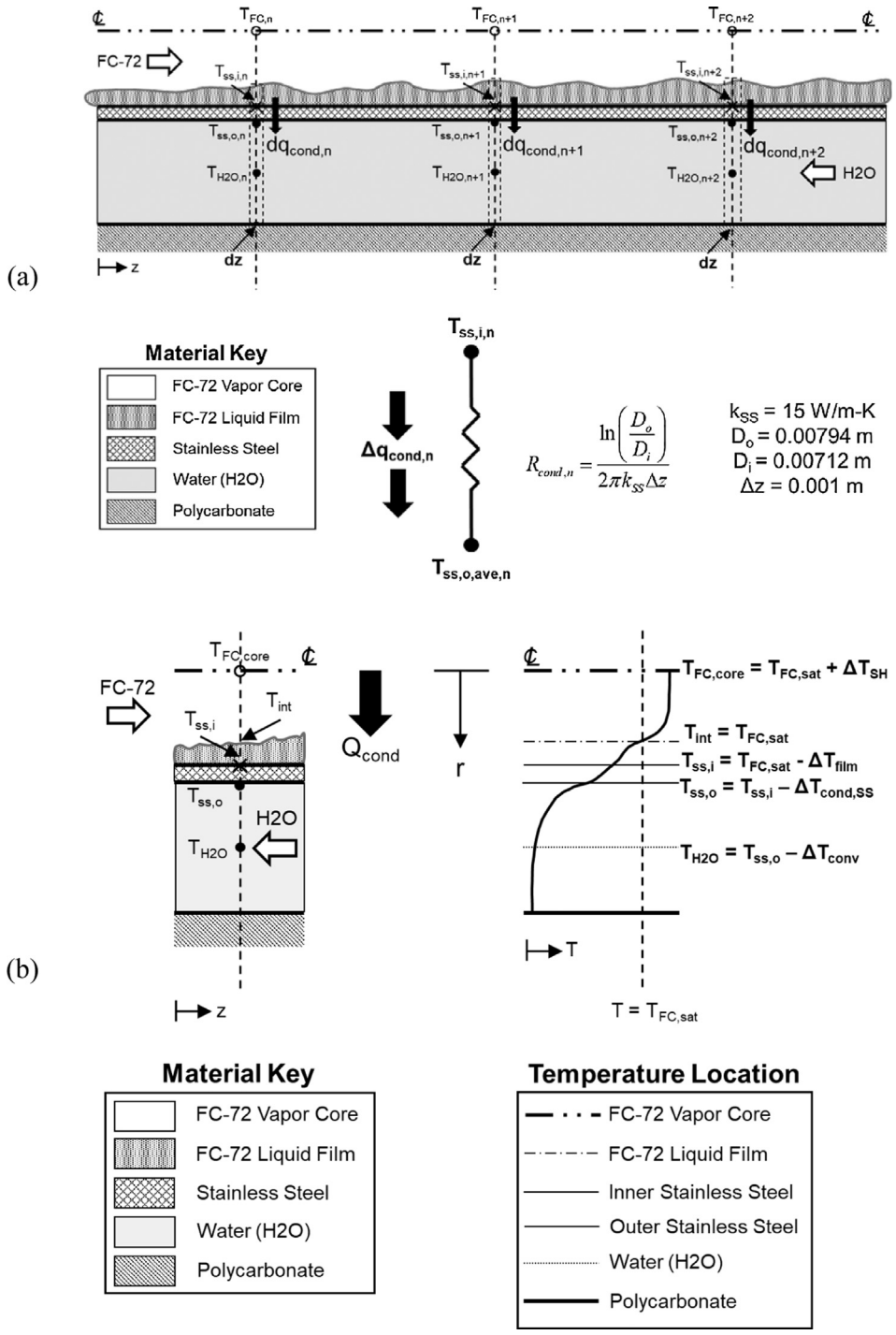

Fig. 4. (a) Schematics for heat transfer coefficient data reduction methodology used here, along with (b) schematic illustrating the importance of capturing radial temperature variations present along the condensation length.

average of the three values is an oversimplification of heat transfer behavior. Because of this horizontal flow cases with mass velocities $G_{FC} \sim 50$ kg/m^2 s and $G_{FC} \sim 100$ kg/m^2 s have been omitted from the current analysis.

The next step in data reduction is to curve fit all 13 water temperature measurements (inlet temperature, exit temperature, and 11 averaged temperatures along the condensation length). This was done using a third order polynomial. Second, third, fourth, and fifth order polynomials were investigated, with second order seen to over-constrain heat flux to a linear variation along the channel length (as condensation heat flux is manifest in the rate of change of water temperatures), while fourth and fifth order polynomials provided similar results to third order but were seen to introduce nonphysical trends in select cases due to overfitting of experimental data. Third order polynomials have also been used in several prior works with great success [35–37,54,55].

Having curve fit water temperatures, it is possible to calculate local incremental energy transfer dq_{cond}. This is equal to the rate of change of water temperature at the measurement location (evaluated by taking the derivative of the water temperature curve fit), and in the present work is evaluated over a 1 mm distance Δz. Formally,

$$\Delta q_{cond,n} = \dot{m}_{H2O} c_{p,f,H2O} \left[\frac{dT_{H2O,fit}}{dz}\right]_n \Delta z, \tag{5}$$

where $\dot{m}_{H2O}$ is water mass flowrate, $c_{p,f,H2O}$ is water specific heat, and n indicates the streamwise location where calculations are taking place (n ranges from 1 to 11). It should be noted here that all fluid properties are evaluated at local pressures assuming a linear variation between inlet and exit values for both water and FC-72 streams.

This local condensation energy transfer may be applied to the broader area surrounding measurement points in order to calculate total energy transferred from condensate (FC-72) to coolant (water). This may be used to update local FC-72 flow quality along the channel length according to the relationship

$$\begin{aligned} x_{e,n+1} &= x_{e,n} - \Delta x_e = x_{e,n} - \frac{Q_{cond,n}}{\dot{m}_{FC} h_{fg,FC}} \\ &= x_{e,n} - \frac{\dot{m}_{H2O} c_{p,f,H2O} (T_{H2O,n} - T_{H2O,n+1})}{\dot{m}_{FC} h_{fg,FC}}, \end{aligned} \tag{6}$$

where $Q_{cond,n}$ refers to the total condensation energy transferred between locations n and $n+1$. Local flow quality is not used in calculation of condensation heat transfer coefficient but becomes important when interpreting local heat transfer trends as well as when calculating channel-average heat transfer coefficient in later analysis.

Once local incremental energy transfer has been calculated based on water temperature change, it is possible to calculate stainless-steel inner surface temperature through a basic conduction network diagram as shown in Fig. 4(a) (making the assumption of steady, radial conduction). This leads to an expression for inner stainless-steel temperature of

$$\begin{aligned} T_{ss,i,n} &= T_{ss,o,n} + \Delta q_{cond,n} R_{conduction,n} \\ &= T_{ss,o,n} + \left[\dot{m}_{H2O} c_{p,f,H2O} (\Delta T_{H2O,n})\right] \left[\frac{\ln(D_o/D_i)}{2\pi k_{ss} \Delta z}\right], \end{aligned} \tag{7}$$

where $R_{conduction,n}$ is the conduction thermal resistance at location n, $\Delta T_{H2O,n}$ is the water temperature derivative as evaluated in Eq. (5), D_o and D_i are outer and inner stainless-steel tube diameters, and k_{ss} is the thermal conductivity of stainless-steel. Values for each of the parameters used in calculating $R_{conduction,n}$ are provided in Fig. 4(a).

Once inner stainless-steel wall temperature has been calculated, condensation heat transfer coefficient is defined as

$$h_{cond,n} = \frac{\Delta q_{cond,n}}{\pi D_i \Delta z (T_{FC,sat,n} - T_{ss,i,n})}, \tag{8}$$

where saturation temperature $T_{FC,sat,n}$ is evaluated at the local condensate pressure (again using an assumed linear variation between measured inlet and exit pressures).

It is worth discussing here the use of $T_{FC,sat}$ to calculate condensation heat transfer coefficient in the portion of the channel where bulk flow is expected to be superheated (i.e., mixed mean temperature is above saturation temperature at the local pressure). In many cases present in the current dataset (corresponding to slightly superheated inlet conditions) this is the case for the first 1–3 measurement locations along the channel length.

Fig. 4(b) provides a schematic of local temperature variation in the radial direction, moving from the adiabatic condition where water meets the polycarbonate wall, across the water and up to the stainless-steel wall, through the stainless-steel wall, across the condensate liquid film, and into the condensate vapor core. It is a fact of the condensation process that, regardless of the amount of superheat present in the vapor core, the interface between liquid and vapor phases will always be maintained at saturation temperature for the local pressure. Because of this the present study uses $T_{FC,sat}$ to calculate condensation heat transfer coefficient at all locations within the condensation length regardless of local superheat (and after the flow has fully condensed heat transfer coefficient is no longer calculated). There are arguments to be made in favor of using local temperature within the superheated region, but regardless of which temperature is chosen, it is imperative that it be clearly stated so values of local heat transfer coefficient may be compared across works.

Fig. 5 presents sample plots showing calculation of condensation heat transfer coefficient for a single test case corresponding to vertical downflow with $G_{FC} = 301.9$ kg/m^2 s, $G_{H2O} = 388.2$ kg/m^2 s, $P_{in} = 128.7$ kPa, $Pwr_{BH} = 1552.7$ W, $x_{e,in} = 1.03$, and $x_{e,out} = 0.13$. Fig. 5(a) shows plots of experimental inlet and exit pressures for both FC-72 (condensate) and water (coolant), along with linear fits used to approximate pressure at intermediate locations.

Fig. 5(b) provides local temperature measurements for FC-72 (with saturation temperature evaluated at local pressure), stainless-steel, and water, with stainless-steel and water temperatures corresponding to averages of circumferentially spaced local measurements as discussed previously. Water temperature curve fit is also shown along with its associated R^2 value. R^2 values for the set of cases used here are always above 0.9, and commonly in the range $R^2 = 0.97$–0.99, indicating water temperatures are well fit by the third order polynomials used.

Calculated inner stainless-steel wall temperature is also shown here, differing by 2–3 °C in the inlet region and near-identical to outer wall temperatures in the exit region (due to a decrease in heat transfer as liquid film thickens in the exit region).

Local FC-72 temperature is plotted along with saturation temperature at the local pressure along the condensation length (with local temperature calculated based on sensible heat change in the upstream, superheated region). It is clear a small difference in values is visible near the first measurement point, after which the bulk flow becomes saturated ($1.00 < x_{e,n} < 0$).

Fig. 5(c) provides values of local condensation heat transfer coefficient, calculated using temperature values shown in Fig. 5(b) and Eq. (8). Values calculated using local FC-72 temperature in the superheated region are plotted separately from those calculated using $T_{FC,sat}$ at all locations. This is done to highlight the small difference in values incurred in the inlet region of the channel (where bulk flow is expected to be superheated) and zero difference along the remainder of the channel length.

Overall, condensation heat transfer coefficient is seen to be high in the inlet region (where liquid film is thinnest), decline along the

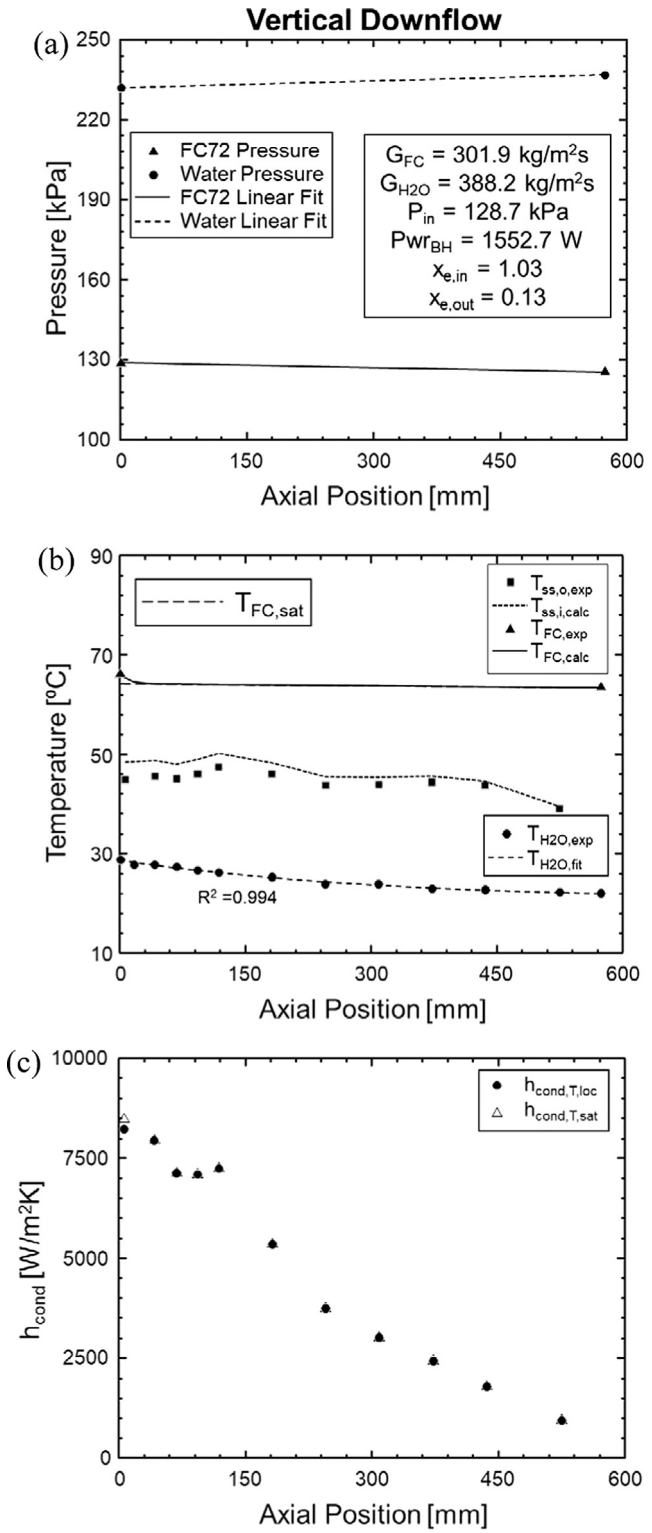

Fig. 5. Values of (a) local pressure and (b) local temperature used to calculate local heat transfer coefficient values shown in (c). Includes comparison between use of local superheated vapor temperature and interface (saturation) temperature to calculate heat transfer coefficient values.

channel length as liquid content increases, and approach a low value in the exit region as flow transitions to single-phase liquid. Investigation of condensation heat transfer parametric trends will be performed in the following section, but first it is necessary to provide additional detail on uncertainty analysis for the present data.

3.3. Condensation heat transfer coefficient uncertainty analysis

To calculate uncertainty associated with condensation heat transfer coefficients it is necessary to recall that Eqs. (8) and (5) combine to define heat transfer coefficient as

$$h_{cond,n} = \frac{\Delta q_{cond,n}}{\pi D_i \Delta z \left(T_{FC,sat,n} - T_{ss,i,n}\right)} = \frac{\dot{m}_{H2O} c_{p,f,H2O} \left[\frac{dT_{H2O,fit}}{dz}\right]_n \Delta z,}{\pi D_i \Delta z \left(T_{FC,sat,n} - T_{ss,i,n}\right)}. \quad (9)$$

While performing heat transfer data reduction the water temperature curve fit derivative is evaluated locally about each measurement point, but to approximate uncertainty associated with this derivative it is more appropriate to treat this derivative as a change in water temperature across a larger Δz centered on each measurement location (meaning values of Δz are small in the upstream region and large in the downstream region). This leads to a relationship of the form

$$h_{cond,n} = \frac{\dot{m}_{H2O} c_{p,f,H2O} \left(T_{H2O,n+1} - T_{H2O,n}\right)}{\pi D_i \Delta z_n \left(T_{FC,sat,n} - T_{ss,i,n}\right)}, \quad (10)$$

which has uncertainty values associated with measurement of water mass flowrate $\dot{m}_{H2O}$, water temperatures $T_{H2O,n+1}$ and $T_{H2O,n}$, FC-72 saturation temperature evaluated at local pressure $T_{FC,sat,n}$, and stainless-steel wall temperature $T_{ss,i,n}$. Tube inner diameter D_i and thermocouple spacing Δz_n are assumed to be exact quantities (as they were measured precisely after fabrication), as is specific heat of cooling water $c_{p,f,H2O}$. Uncertainty for local condensation heat transfer coefficient may then be calculated as

$$\left[\frac{U_h}{h_{cond,n}}\right]^2 = \left[\frac{U_{\dot{m}}}{\dot{m}_{H2O}}\right]^2 + 2\left[\frac{U_{T,H2O}}{T_{H2O,n+1} - T_{H2O,n}}\right]^2 + \left[\frac{U_{T,FC,sat}}{T_{FC,sat,n} - T_{ss,i,n}}\right]^2 + \left[\frac{U_{T,ss}}{T_{FC,sat,n} - T_{ss,i,n}}\right]^2, \quad (11)$$

where U_h, $U_{\dot{m}}$, $U_{T,H2O}$, $U_{T,FC,sat}$, and $U_{T,ss}$ are the uncertainties of local condensation heat transfer coefficient, water mass flowrate, water temperature measurements, calculated FC-72 saturation temperature at the local pressure, and stainless-steel wall temperature measurements, respectively. U_h is the parameter being solved for, but all other uncertainties are defined as $U_{\dot{m}} = 0.002\dot{m}_{H2O}$, $U_{T,H2O} = 0.1$ °C, $U_{T,FC,sat} = 0.2$ °C, and $U_{T,ss} = 0.3$ °C. Water and stainless-steel wall temperatures are measured using type-E thermocouples with manufacturer stated uncertainties of ±0.4 °C (as mentioned in Section 2), but these sensors went through extensive calibration in NASA Glenn Research Center's calibration lab prior to use, and post-calibration uncertainties are reflected in the values provided above.

Eq. (11) was evaluated for every set of operating conditions tested, and Fig. 6(a) provides local uncertainty results for a subset of data corresponding to all cases with superheated (or near-superheated) inlet conditions. Local values calculated for each set of operating conditions were averaged (over all operating conditions) at each axial measurement location, providing representative values of uncertainty as a function of position along the channel length.

It is clear uncertainty is low in the upstream region, with values for each of the three orientations falling near 25%. This gradually increases for successive measurement points until the sixth measurement station, where spacing between successive temperature measurements becomes larger and uncertainty drops. Near the exit of the channel, however, uncertainty increases significantly, approaching values of 100% for the final three measurement locations.

All variation in local uncertainty values may be explained by the dominant contribution of water temperature measurement on overall uncertainty value. The denominator of the second term on the right-hand side of Eq. (11), $T_{H2O,n+1}$ - $T_{H2O,n}$, is often on the

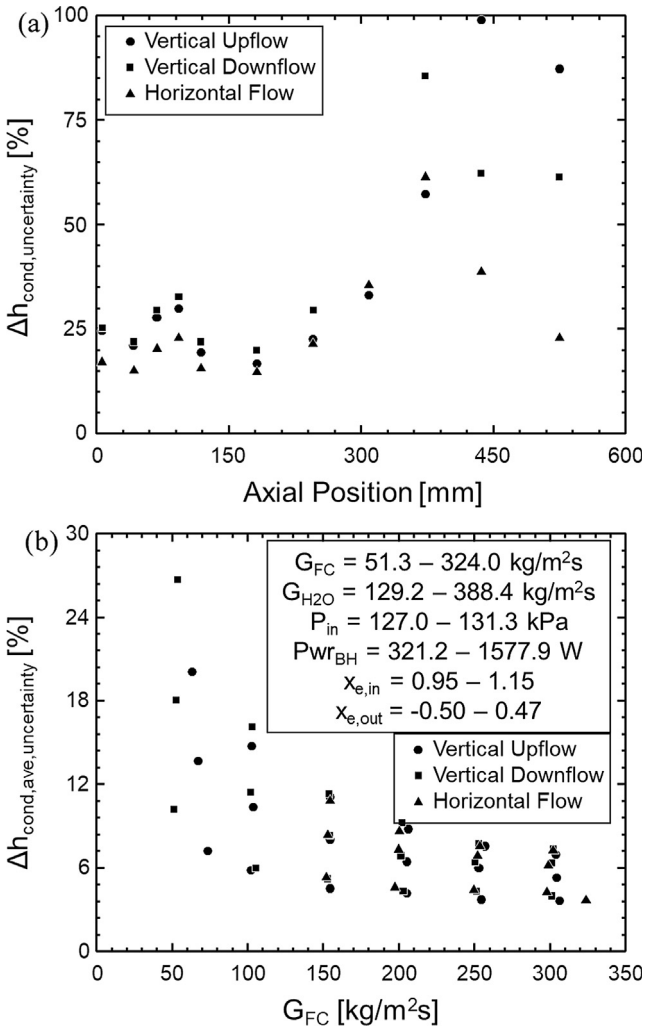

Fig. 6. Uncertainty of (a) local heat transfer coefficient calculations averaged over all cases with superheated vapor inlet conditions (inset in Fig. 6(b)) versus measurement position, and (b) uncertainty of channel length average heat transfer coefficient values versus FC-72 mass velocity.

same order of magnitude as measurement uncertainty for each thermocouple (~0.1–1 °C), meaning that term is the primary source of uncertainty in condensation heat transfer coefficient calculation. Recalling the plot of water temperatures versus position in Fig. 5(b), water temperatures change relatively rapidly in the upstream region, meaning the difference in successive values is high and their contribution is low. Temperatures change more slowly near the FC-72 exit, but spacing between points is increased, resulting in the drop in uncertainty near the sixth measurement station. Near the FC-72 exit (and water inlet), however, there are near-zero changes in water temperature, resulting in the high uncertainty values shown in Fig. 6(a).

These trends regarding uncertainty of local measurements should be kept in mind when analyzing local heat transfer trends in the following section but are not the only calculated uncertainties to keep in mind. The parameter most frequently of interest when analyzing condensing systems is channel average heat transfer coefficient $h_{cond,ave}$, defined analytically as

$$h_{cond,ave} = \frac{1}{L_{cond}} \int_0^{L_{cond}} h(z)dz, \tag{12}$$

where the condensation length L_{cond} is defined as the portion of the channel with quality $1.00 < x_{e,loc} < 0$. In the present scheme, average condensation heat transfer coefficient is calculated numerically according to the relationship

$$h_{cond,ave} = \frac{1}{L_{cond}} \sum_{i=1}^{n_{cond}} h_{cond,n} \Delta z_n, \tag{13}$$

where Δz_n is the local distance centered between consecutive measurement points along the condensation length and n_{cond} is the number of measurement locations with local qualities $1.00 < x_{e,loc} < 0$ for each test case. It should be noted that n_{cond} as well as the physical locations of n_{cond} shift depending on whether inlet conditions are slightly superheated or saturated mix.

Propagating uncertainty associated with local condensation heat transfer coefficients $h_{cond,n}$ through Eq. (13) is done by evaluating the expression

$$\frac{U_{h,ave}}{h_{cond,ave}} = \frac{1}{L_{cond}} \left(\sum_{i=1}^{n_{cond}} E_{cond,i}^2 \Delta z_i^2 \right)^{1/2}, \tag{14}$$

where $E_{cond,i}$ is the absolute error associated with each local heat transfer coefficient measurement (relative value as shown in Fig. 6(a) multiplied by local heat transfer coefficient value).

For the same cases as plotted in Fig. 6(a), (b) displays uncertainty of average heat transfer coefficient plotted versus FC-72 mass velocity for all three orientations tested. Uncertainty reaches its maximum value of ~25% for low mass velocity cases, decreasing to ~5% for higher mass velocity cases. This is again due to the role of water temperature measurement dominating heat transfer coefficient uncertainty: Cases with high G_{FC} have larger associated condensation heat transfer, leading to larger temperature gradients on the water side which reduce uncertainty.

At each FC-72 mass velocity results for three different water mass velocities are shown. In each case the highest measurement uncertainty is associated with the highest water mass velocity, as these cases have the smallest water temperature change along the heated length. This would indicate low water flowrate cases as desirable, but as will be seen when analyzing heat transfer results, low uncertainty must be balanced with the need for water-independent heat transfer measurement (requiring high water heat transfer coefficients and thus high water flowrates).

Moving forward, heat transfer results will be presented without error-bars, as these unnecessarily crowd figures and make interpretation difficult. Thus, it is important to use the information presented in this subsection when analyzing heat transfer results presented hereafter. Low-uncertainty results (channel-averaged results, local results at the channel inlet) may be interpreted with confidence, while high-uncertainty results (local results at the channel exit) should only be interpreted with care.

4. Heat transfer results

Having provided details on condensation heat transfer coefficient data reduction and uncertainty analysis, it is now time to investigate condensation heat transfer coefficient trends.

4.1. Local results

Fig. 7 provides plots of local heat transfer coefficient versus axial position along the condensation length for each orientation. Fig. 7(a) shows plots corresponding to all mass velocity cases with superheated vapor inlet conditions, Fig. 7(b) provides plots of high mass velocity (G_{FC} ~ 300 kg/m^2 s) with multiple inlet qualities, and Fig. 7(c) low mass velocity (G_{FC} ~ 100 kg/m^2 s) with multiple inlet qualities. There is no horizontal data in Fig. 7(c) due to the omission of low flowrate horizontal cases (as discussed in the preceding

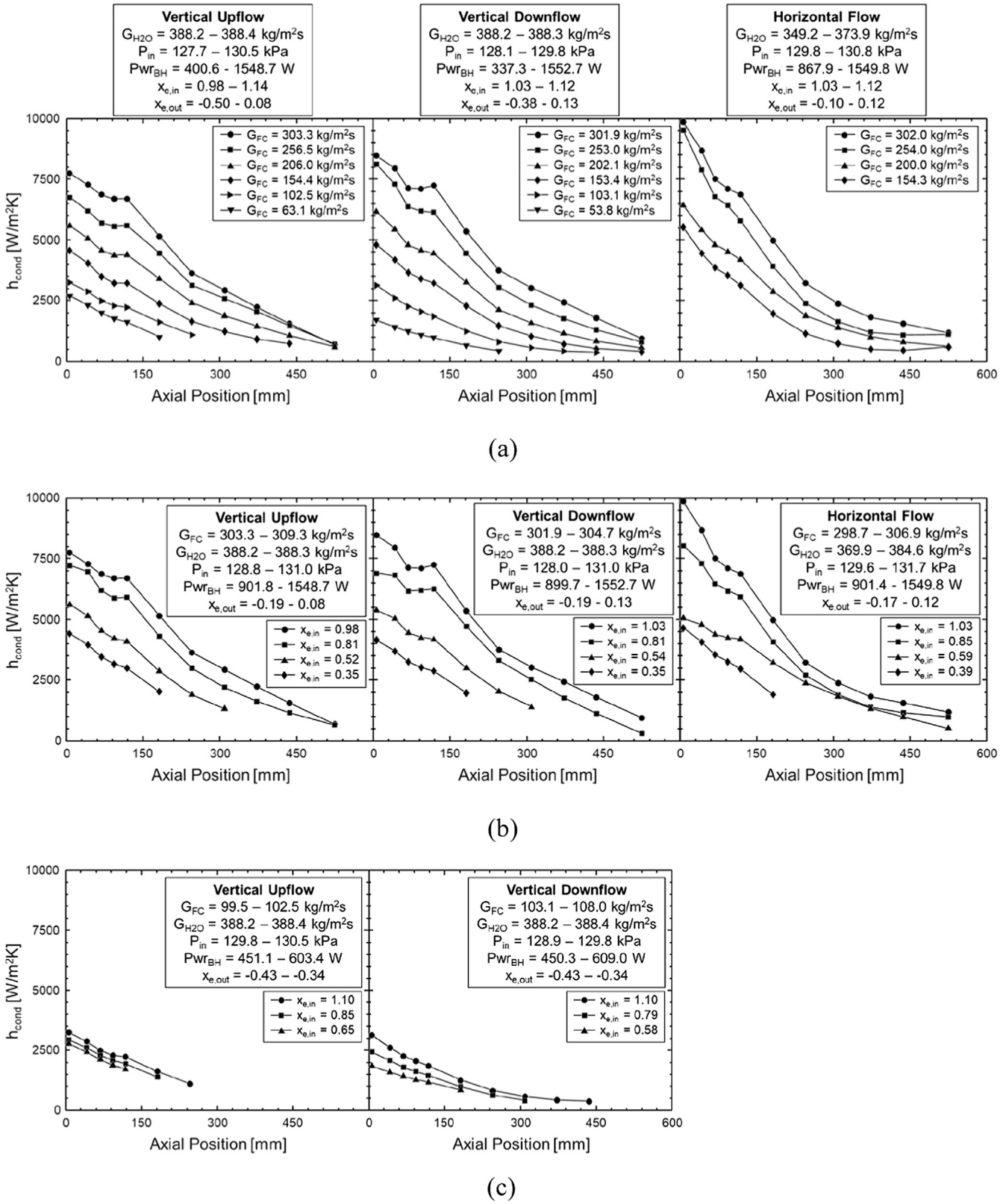

Fig. 7. Evaluation of heat transfer coefficient versus axial location for all three orientations with (a) multiple flowrates and $x_{e,in} \sim 1.05$, (b) multiple inlet qualities and $G_{FC} \sim 300$ kg/m^2 s, and (c) multiple inlet qualities and $G_{FC} \sim 100$ kg/m^2 s.

section). It should also be noted that all cases presented in Fig. 7 correspond to the highest water mass velocity.

Fig. 7(a) shows that, for all orientations and flowrates, condensation heat transfer is at its maximum value in the upstream region of the channel. The liquid film here is at its thinnest which leads to highly efficient condensation heat transfer. Towards the channel exit significant liquid film thickening has occurred which leads to decreased condensation heat transfer. For some of the lower flow-

rate cases full condensation is achieved prior to the channel exit, and heat transfer coefficient for locations past this point are not calculated.

Fig. 7(b) provides similar results, now for a single mass velocity $G_{FC} \sim 300$ kg/m^2 s with different curves on the same plots representing changes in channel inlet quality (corresponding to target values of $x_{e,in} \sim 1.00$, 0.80, 0.60, and 0.40). Local heat transfer coefficient values in each orientation are seen to be highest for the highest quality cases and decrease as inlet quality decreases. This result makes sense intuitively as lower inlet quality cases possess thicker liquid films which reduce local condensation heat transfer coefficient.

Fig. 7(c) shows results for low mass velocity ($G_{FC} \sim 100$ kg/m^2 s) with multiple inlet qualities. Differences between inlet qualities is significantly reduced compared to that seen in Fig. 7(b) for high mass velocity cases. This indicates inlet quality has a secondary effect on condensation heat transfer coefficient, with mass velocity playing a dominant role.

Across Fig. 7(a)–(c), the influence of orientation is most noticeable at low mass velocities. For cases with $G_{FC} \sim 50$ and 100 kg/m^2 s, vertical upflow is seen to exhibit higher local heat transfer coefficient values than vertical downflow. This can be attributed to the presence of a counter-current flow regime in upflow condensation for these operating conditions (as discussed in Fig. 3) leading to significant liquid film breakup and periodic transport of liquid through the condensation length. Vertical downflow cases for these operating conditions are expected to exhibit a smooth liquid film along the entire condensation length with liquid transport primarily due to body force. Although a more stable operating condition (in terms of mass velocity and pressure fluctuations), this configuration is seen to yield lower overall heat transfer coefficient values.

For higher mass velocity cases, results across the three orientations become similar. The only exceptions are heat transfer coefficient values calculated at the first (upstream) measurement location for horizontal flow, which is noticeably higher than its vertical upflow and downflow counterparts. In the downstream region behavior becomes near identical to that for upflow and downflow orientations, however, meaning this upstream enhancement is a localized phenomenon. It should also be noted that this difference for horizontal flow falls within the uncertainty band outlined in Fig. 6(a), meaning it should not be interpreted as a physical phenomenon.

Fig. 8 again provides plots of local condensation heat transfer coefficient, this time plotted versus local quality (as calculated by Eq. (6), corresponding to quality at each of the 11 measurement locations). Only locations with qualities in the range $1.00 < x_{e,n} < 0$ are shown in the present plots. Fig. 8(a), (b), and (c) correspond to vertical upflow, vertical downflow, and horizontal flow orientations, respectively. Each subplot within the subfigures shows results for multiple mass velocities with inlet qualities of $x_{e,in} \sim 1.00$, $x_{e,in} \sim 0.80$, and $x_{e,in} \sim 0.50$, moving from left to right.

Fig. 8(a) clearly shows values of heat transfer coefficient decreasing as local quality decreases, similar to the conclusion drawn when analyzing Fig. 7. Additionally, the trend of decreased heat transfer coefficient for decreasing mass velocity is again present, although only noticeable at high local qualities. As local quality decreases differences between mass velocities are reduced, with heat transfer coefficient values corresponding to near-zero qualities exhibiting almost no differences across the full mass velocity range.

As discussed when comparing Fig. 7(b) and (c), differences in heat transfer coefficient for different mass velocities are most pronounced for high local qualities. This is likely due to the dominant role of interfacial shear (provided by the fast-moving vapor core) for these regions where the liquid film is thinnest. As liquid film thickness increases liquid inertia becomes more appreciable and interfacial shear stress plays a less influential role in advecting the liquid film, leading to smaller differences in heat transfer coefficient for different mass velocities.

It is also important to recall when analyzing differences in heat transfer coefficient for the low quality region that these measurements often correspond to the exit region of the channel, which Fig. 6(a) showed possessing significant uncertainty. Thus, these results should be interpreted with caution in the present study.

Across all three orientations shown in Fig. 8, differences in orientation are again most visible for low mass velocity cases, with vertical upflow cases exhibiting higher heat transfer coefficient values compared to vertical downflow counterparts. For higher mass velocity cases all three orientations yield similar values for local condensation heat transfer coefficient as a function of local quality.

It should be noted that comparison of heat transfer coefficient values for fixed orientation, mass velocity, and local quality, but with differing inlet quality (moving horizontally across Fig. 7(a), (b), or (c)), indicates differences in value. Practically, this indicates a dependence of heat transfer coefficient on the axial location where the measurement was made: In a purely theoretical case this should not be true, but practical considerations (i.e. change in local pressure with position, change in wall temperature due to changes in cooling water temperature, differences in uncertainty with position as discussed in Fig. 6) mean values may exhibit slight differences.

4.2. Channel-average results

Prior to discussing parametric trends for channel-averaged condensation heat transfer coefficient, it is first necessary to comment on the impact of water mass velocity on overall condensation within the test section. Fig. 9 provides plots of channel averaged heat transfer coefficient (left, calculated using Eq. (13)) and total condensation heat transfer (right) versus cooling water mass velocity G_{H2O}. All results prior to this point have corresponded to maximum cooling water mass velocity of $G_{H2O} \sim 388$ kg/m^2 s, but three different water flowrates were tested (as outlined in Table 1) to determine ability of the current test section to offer condensation heat transfer results independent of cooling water flowrate. If water flowrate is high enough heat transfer coefficient on the condensate side will become the limiting thermal resistance and heat transfer results will not change for increase in water flowrate.

Fig. 9(a) shows that, for vertical upflow condensation, cases with low condensate (FC-72) mass velocity exhibit little-to-no changes in condensation heat transfer for changes in cooling water mass velocity. As condensate mass velocity increases, however, channel average heat transfer coefficient and total condensation heat transfer are seen to decrease and increase, respectively, for increases in cooling water mass velocity. Moderate values of G_{FC} appear to plateau between $G_{H2O} \sim 260$–390 kg/m^2 s, but high values of G_{FC} exhibit changes in heat transfer all the way through peak values of G_{H2O}. This decrease in heat transfer coefficient is likely attributable to a lowering of the stainless-steel wall temperature by faster water flow.

Similar conclusions may be drawn when analyzing results for vertical downflow and horizontal flow orientations in Fig. 9(b) and (c), respectively. Based on this, data presented for the remainder of this section will correspond only to cases with (i) $G_{H2O} \sim 390$ kg/m^2 s, (ii) $G_{H2O} \sim 260$ kg/m^2 s with $G_{FC} \leq 150$ kg/m^2 s, and (iii) $G_{H2O} \sim 130$ kg/m^2 s with $G_{FC} \leq 100$ kg/m^2 s, done to ensure heat transfer results are water-side independent (or as close as possible using the current dataset). It is expected the final ISS experiment test matrix will include cases with higher water mass velocity ($G_{H2O} \sim 520$ kg/m^2 s), done to help further ensure water-side independence of condensation results.

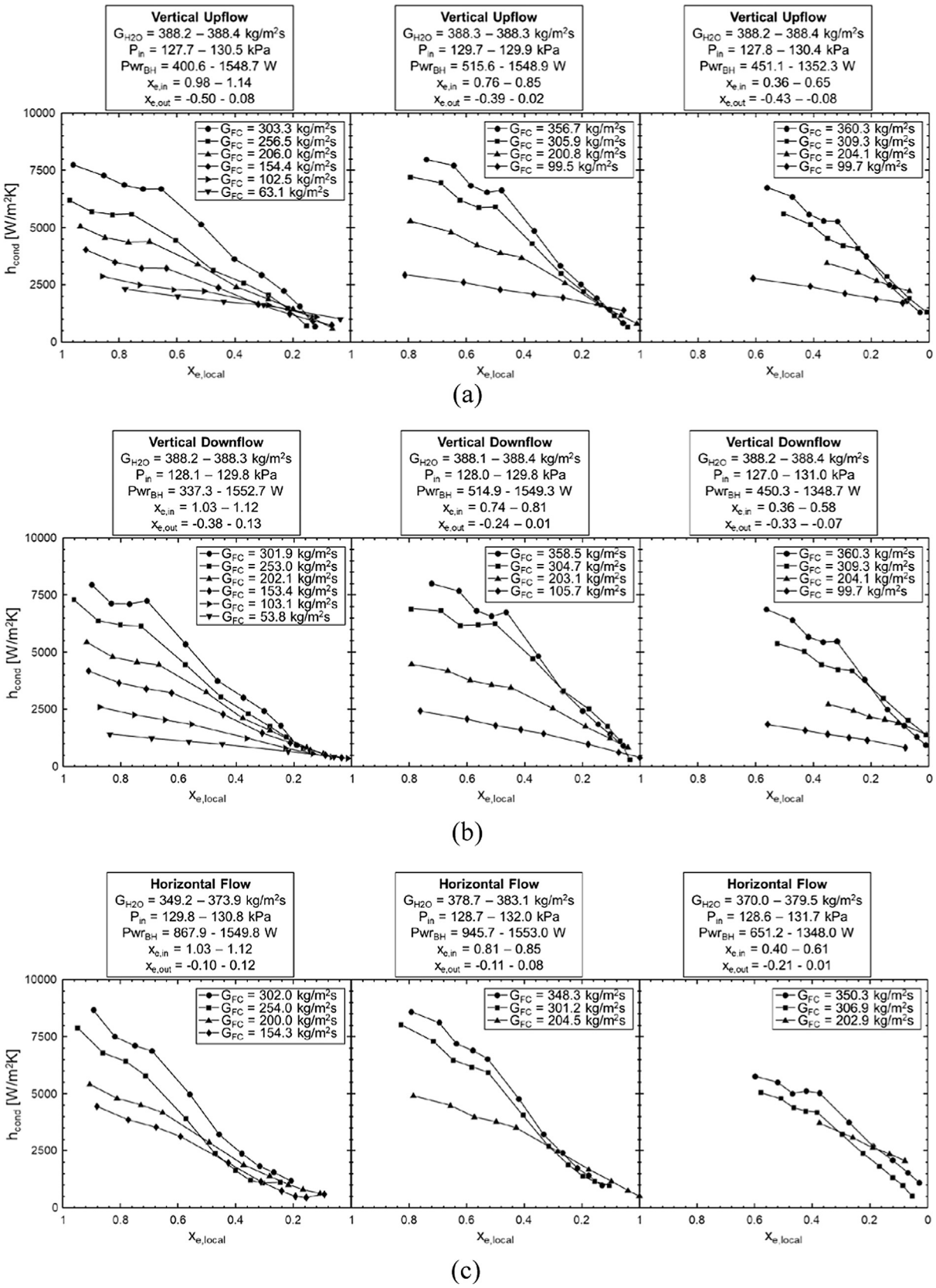

Fig. 8. Evaluation of heat transfer coefficient versus local quality for multiple mass velocities with (from left to right) $x_{e,in} > 1.00$, $x_{e,in} \sim 0.80$, and $x_{e,in} \sim 0.60$, in (a) vertical upflow, (b) vertical downflow, and (c) horizontal flow orientations.

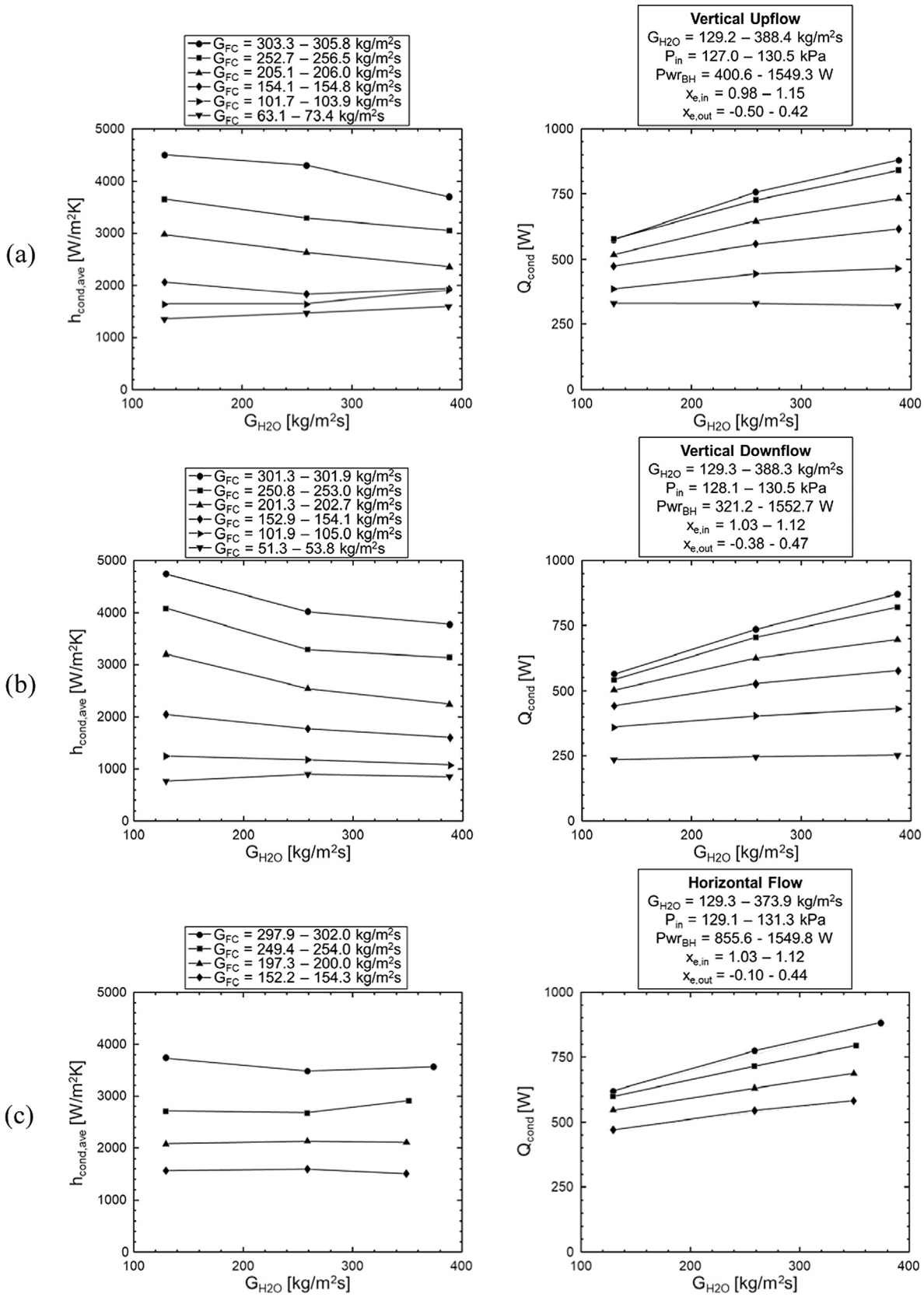

Fig. 9. Plots of channel-average condensation heat transfer coefficient and total condensation energy transfer versus cooling water mass velocity for (a) vertical upflow, (b) vertical downflow, and (c) horizontal flow orientations.

Fig. 10 provides plots of average heat transfer coefficient (using the water-independent subset of data) versus FC-72 mass velocity for each orientation tested. Separate curves on each plot correspond to different water mass velocities tested, and the fact these curves collapse well verifies the subset outlined in the preceding paragraph is composed of water-independent condensation results.

Comparison between Fig. 10(a) and (b), corresponding to vertical upflow and downflow orientations, reinforces the trend first discussed alongside Fig. 7, that at low FC-72 mass velocities upflow heat transfer is higher than downflow. As mass velocity increases, however, values of channel-length average heat transfer coefficient become similar for all three orientations (including horizontal flow in Fig. 10(c)).

Fig. 11 provides similar plots for each orientation, this time of channel average heat transfer coefficient versus FC-72 inlet quality for each case. Curves on each plot represent similar values of FC-72 mass velocity, and only the highest water mass velocity of $G_{H2O} \sim 390$ kg/m^2 s is represented in this figure.

Trends related to changes in inlet quality are not as straightforward to interpret as those for FC-72 mass velocity. In the majority of cases, increasing inlet quality from a low value towards $x_{e,in} = 1.00$ results in increased heat transfer coefficient (seen for most FC-72 mass velocities in Fig. 11(a) and (b) corresponding to vertical upflow and downflow). Above $x_{e,in} = 1.00$, however, average heat transfer coefficient is seen to decrease for increasing $x_{e,in}$. This is likely due to using only points with $1.00 < x_{e,loc} < 0$ when calculating channel-average heat transfer coefficient, which results in

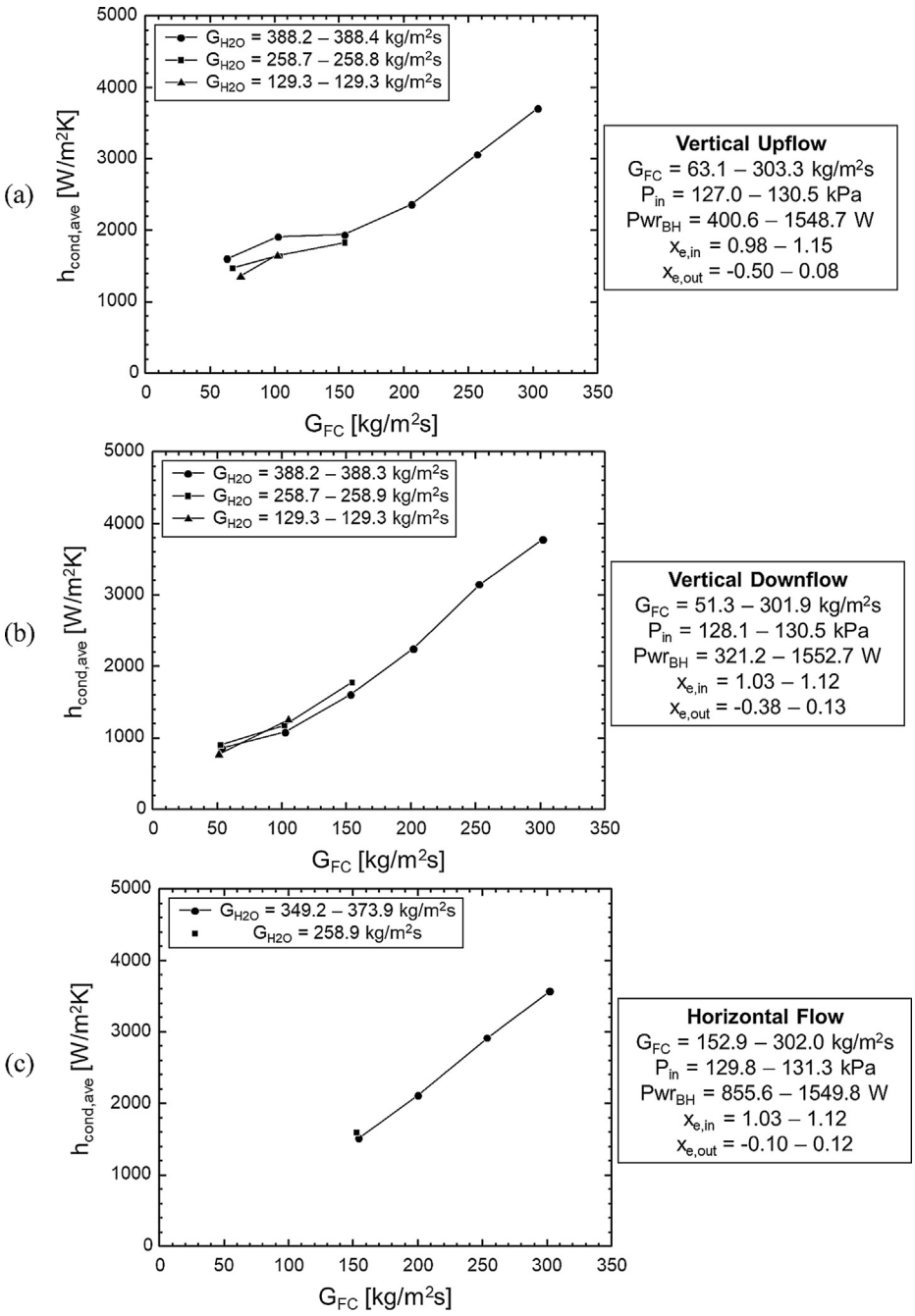

Fig. 10. Evaluation of condensation length average heat transfer coefficient versus FC-72 mass velocity for (a) vertical upflow, (b) vertical downflow, and (c) horizontal flow orientations.

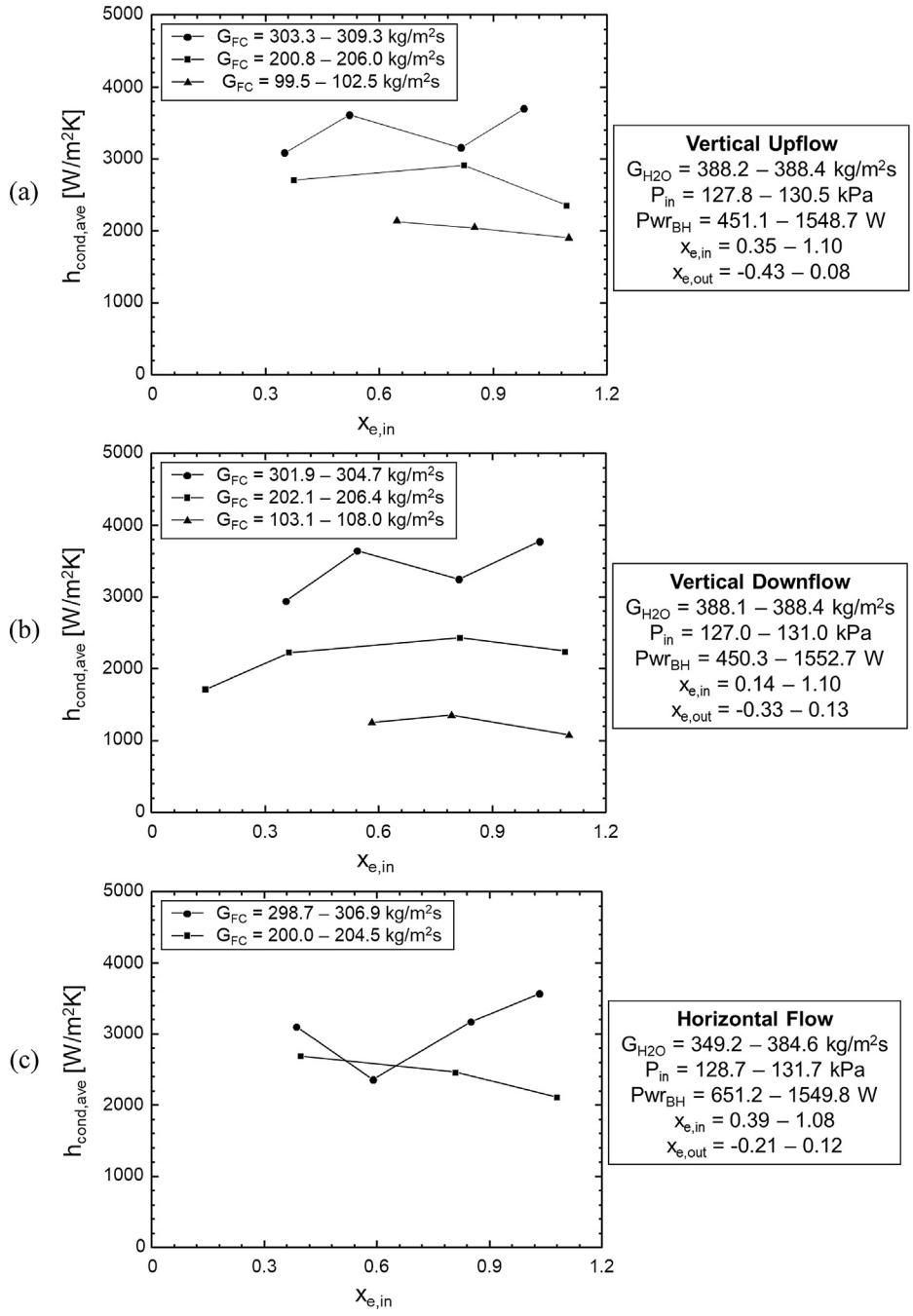

Fig. 11. Evaluation of condensation length average heat transfer coefficient versus FC-72 inlet quality for (a) vertical upflow, (b) vertical downflow, and (c) horizontal flow orientations.

some upstream measurement locations being neglected when calculating channel average heat transfer coefficient for cases with superheated vapor inlet conditions.

Across Figs. 7–11 (presenting both local and channel averaged values for condensation heat transfer coefficient), mass velocity (flow inertia) is seen to be the dominant parameter affecting values of condensation heat transfer coefficient. Higher flow inertia is seen to lead to higher condensation rate in all cases. Flow quality is also seen to influence condensation heat transfer coefficient, with lower quality cases/locations (meaning more liquid is present) exhibiting lower heat transfer rate due to reduced interfacial area and lower temperature gradient between vapor condensate and tube surface (due to the presence of thick liquid film).

When comparing heat transfer results across the three orientations investigated heat transfer behavior is seen to be near-identical for high mass velocity cases, while at low mass velocities heat transfer behavior differs significantly between orientations. These orientation effects are investigated in more detail in the following subsection.

4.3. Influence of body force

As discussed in the introduction, conducting flow condensation tests at multiple orientations in Earth's gravity is one method for investigating the influence of body force on flow condensation heat transfer. This 1-g data will be analyzed alongside microgravity data

to be collected on the ISS by the Flow Boiling and Condensation Experiment (FBCE) to provide a more complete analysis of body force effects, but for now important conclusions may still be drawn from analysis of 1-g data.

Fig. 12(a) provides a plot of channel average heat transfer coefficient versus mass velocity for all three orientations. At low mass velocities (for which horizontal cases are omitted due to their non-axisymmetric nature) clear differences are seen between vertical upflow and downflow orientations, with upflow exhibiting higher heat transfer coefficient values. In a recent study by O'Neill et al. [62] a similar plot was provided for condensation of FC-72 in a larger tube (D_i = 11.89 mm, L_{cond} = 807.7 mm). Differences in condensation heat transfer across orientations was again most pronounced at low mass velocities, but in their work vertical downflow was seen to exhibit peak condensation heat transfer coefficient while the present study clearly shows vertical upflow exhibiting the highest values of heat transfer coefficient.

Additionally, values of heat transfer coefficient for the three orientations are seen to converge at a lower mass velocity ($G_{FC} \sim 200$ kg/m^2 s) in the present study as opposed to the value of $G_{FC} \sim 400$ kg/m^2 s seen in the prior work [62]. These differences are likely due to the heightened influence of surface tension in the present test section, which possesses a hydraulic diameter of D_i = 7.12 mm.

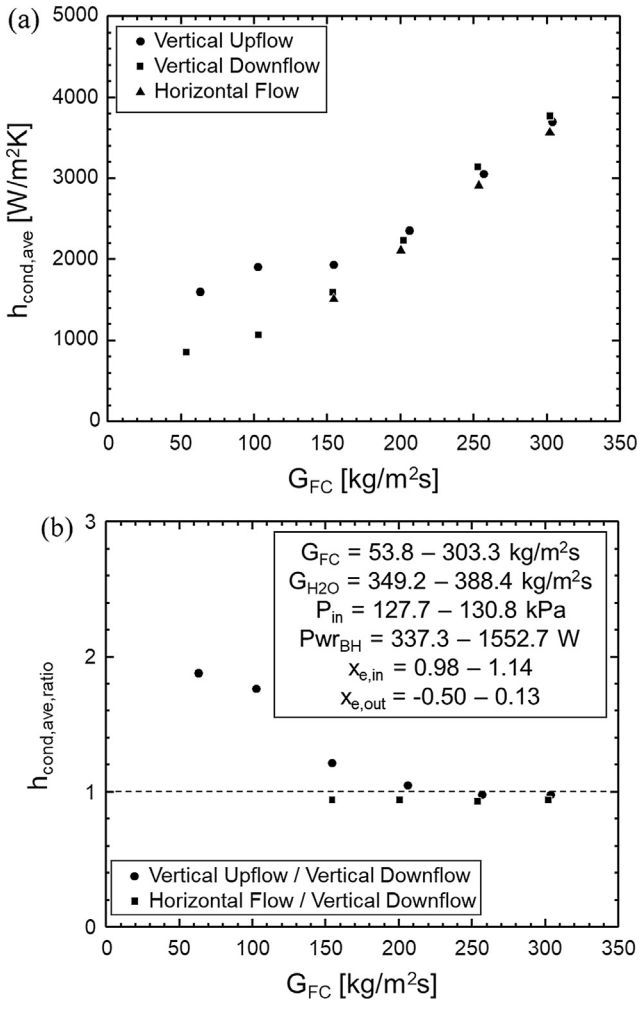

Fig. 12. (a) Average condensation heat transfer coefficient versus mass velocity for three water flowrates in all three orientations, and (b) ratio of Vertical Upflow and Horizontal Flow (respectively) to Vertical Downflow average heat transfer coefficient, showing the effect of increases in mass velocity on converging values.

Fig. 12(b) plots ratios of vertical upflow to downflow and horizontal to downflow heat transfer coefficients for each mass velocity. For the present test section vertical upflow is seen to exhibit heat transfer coefficient nearly double that of vertical downflow, with values converging near $G_{FC} \sim 200$ kg/m^2 s (as mentioned when analyzing Fig. 12(a)). Horizontal flow values, only included for cases with $G_{FC} \geq 150$ kg/m^2 s, are seen to be near identical to vertical downflow values at the outset. It is expected results for lower mass velocities (where stratified flow is present) would diverge.

It should be noted here that the mass velocity for which vertical upflow and downflow results begin to converge, $G_{FC} \sim 200$ kg/m^2 s, is very close to the transition to co-current annular vertical upflow established in the companion study [74] and presented in Fig. 3 here. Similarly, horizontal flow condensation heat transfer is seen to converge with vertical downflow at $G_{FC} \sim 150$ kg/m^2 s, which is near the transition point between stratified and axisymmetric flow outlined in the companion study [74] and Fig. 3 here.

Physically, this means cases with annular, co-current flow exhibit body force independent heat transfer. The prior study by O'Neill et al. [62] developed a set of mechanistic criteria for determining mass velocity required for body force independent heat transfer as a function of relevant dimensionless groups. Two are used, one assessing the influence of body force parallel (or opposite) to flow direction, and the other determining the impact of body force perpendicular to flow direction (i.e., leading to stratification at low mass velocities in horizontal flow). The first, dealing with the influence of body force parallel to flow, is of the form

$$|Fr| = \frac{0.235}{aRe_c^n}, \tag{15}$$

where Fr is Froude number, Re_c is vapor core Reynolds number, and a and n are constants. These are defined as (respectively)

$$Fr = \frac{\rho_g}{\rho_f}\frac{\left(\bar{u}_g - u_i\right)^2}{g\sin(\theta)D_F}, \tag{16}$$

$$Re_c = \frac{\rho_g\left(\bar{u}_g - u_i\right)(D_h - 2\delta)}{\mu_g}, \tag{17}$$

$$\begin{aligned} &a = 16,\ n = -1 \text{ for } 0 \leqslant Re_c < 2000 \\ &a = 0.079,\ n = -0.25 \text{ for } 2000 \leqslant Re_c < 20,000 \\ &a = 0.046,\ n = -0.20 \text{ for } 20,000 \leqslant Re_c \end{aligned} \tag{18}$$

where $\bar{u}_g$ is mean vapor velocity, u_i is interfacial velocity, g is Earth's gravitational constant, D_F is film diameter, θ is test section orientation, δ is film thickness, and constants defined by Eq. (18) are according to Shah and London [83].

The second criterion, dealing with the influence of body force perpendicular to flow direction, is defined as

$$\frac{|Bo|}{We^2} = 5.12 \times 10^{-5}, \tag{19}$$

where Bo is Bond number and We is Weber number, defined as

$$Bo = \frac{\left(\rho_f - \rho_g\right)g\cos(\theta)L_{char}^2}{\sigma}, \tag{20}$$

And

$$We = \frac{\left(\rho_f''\rho_g''\right)\left(\bar{u}_g - \bar{u}_f\right)^2 L_{char}}{\left(\rho_f'' + \rho_g''\right)\sigma}. \tag{21}$$

In these equations $\bar{u}_f$ is mean liquid velocity, ρ_f'' and ρ_g'' are modified liquid and vapor densities, and L_{char} is a characteristic length scale which cancels in Eq. (19).

Values on the right hand side of Eq.'s (15) and (19) are transition points (with criteria values less than the RHS indicating gravity independent heat transfer) determined using the original dataset. For full details on the development of these criteria and how they may be evaluated the original reference should be consulted [62].

Fig. 13(a) and (b) provide plots of these dimensionless criteria (for Eq.'s (15) and (19), respectively) plotted versus mass velocity using operating conditions for the present study. The bold parameters in each inset are those actually used by the criteria (mass velocity, pressure for properties calculation, and exit quality limited to values $x_{e,out} \geq 0.15$ due to formulation of the criteria [62]).

Fig. 13(a) shows that, for vertical upflow and downflow data, gravity independence is predicted by $G_{FC} \sim 125$ kg/m^2 s. This is slightly less than the $G_{FC} \sim 200$ kg/m^2 s observed in the present experiments. For horizontal flow, Fig. 13 (b) does not predict gravity independence until $G_{FC} \sim 300$ kg/m^2 s, which is higher than the $G_{FC} \sim 150$ kg/m^2 s observed experimentally.

In both cases predictions are slightly off from experimentally observed convergence points in Fig. 12. Despite this Fig. 13(a) and (b) do a good job of capturing experimental trends of convergence towards gravity independence and provide a good qualitative measure of gravity independence for the present dataset. It is expected that future work re-evaluating these gravity independence criteria on a more generalized dataset (including data for different working fluids and test sections) may provide more robust predictions of gravity independence.

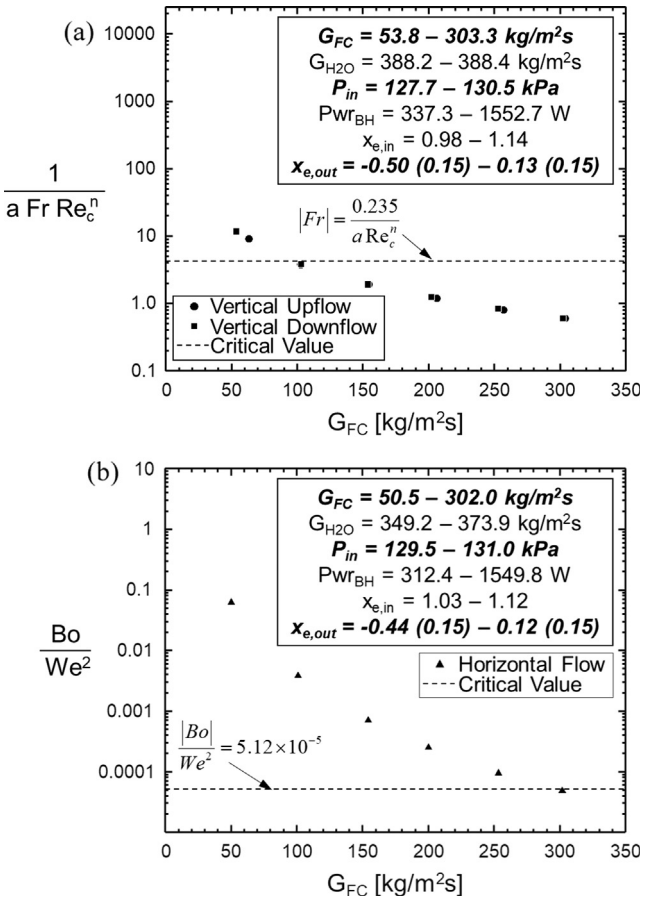

Fig. 13. Evaluation of gravity independence criteria developed by O'Neill et al. [62] using the current data. Subfigures correspond to the influence of body force acting (a) parallel or opposite to flow direction and (b) perpendicular to flow direction.

5. Evaluation of predictive models

Having presented experimental results for flow condensation heat transfer coefficient in vertical upflow, vertical downflow, and horizontal flow orientations, it is now possible to use the data to evaluate common predictive models present in literature. Before beginning evaluation, it should be noted that only experimental cases using the highest water mass velocity ($G_{H2O} \sim 390$ kg/m^2 s) are presented here to ensure water-independent (or as close as possible) heat transfer results are used.

Analysis in this section will be segmented based on channel orientation, as different tools are recommended for different flow orientations.

5.1. Separated Flow Model (SFM) predictions for vertical downflow

Originally developed by Kim and Mudawar [84] for prediction of flow condensation in parallel micro-channel heat sinks, the Separated Flow Model (SFM) for annular condensation has since been adapted and used in several studies investigating flow condensation in single circular tubes similar to the current test geometry [35,54,62]. Table 2 provides a full list of model equations as formulated for flow in mini-channels at variable orientation, and details on solution procedure may be found in the original work [84].

Although capable of providing predictions for flow at any orientation, as currently constructed the model provides best predictions for vertical downflow condensation. Fig. 14 provides six plots comparing local condensation heat transfer coefficient to predictions ((a)–(f)), as well as a plot (Fig. 14(g)) providing ratio of predicted to experimental channel-average heat transfer coefficient values for all 17 test cases used.

Fig. 14(a) shows that, for high G_{FC} and slightly superheated inlet conditions, the SFM under-predicts heat transfer coefficient in the upstream portion of the channel, although downstream results show closer agreement. Successive decreases in G_{FC} in Fig. 14(b) and (c) lead to closer agreement in both upstream and downstream portions of the channel.

Fig. 14(d) provides results for high G_{FC} with two-phase mixture inlet conditions. Heat transfer coefficient is again underpredicted in the upstream portion of the channel, but to a lesser degree than that seen in Fig. 14(a) corresponding to superheated vapor at the channel inlet. Similar to the trend seen for Fig. 14(b) and (c), decreases in G_{FC} for Fig. 14(e) and (f) lead to closer agreement between predicted and experimental heat transfer coefficient values.

Ratios of predicted to experimental channel-average heat transfer coefficient values in Fig. 14(g) are plotted versus liquid only Reynolds number, Re_{fo}, and turbulent-turbulent Martinelli parameter, X_{tt}, defined as

$$Re_{fo} = \frac{G_{FC} D_i}{\mu_f}, \tag{22}$$

and

$$X_{tt} = \left(\frac{1-x}{x}\right)^{0.9} \left(\frac{\rho_g}{\rho_f}\right)^{0.5} \left(\frac{\mu_f}{\mu_g}\right)^{0.1}, \tag{23}$$

respectively. These two dimensionless groups were selected as they both commonly appear in correlations for condensation heat transfer coefficient and allow assessment of predictive ability for differences in flow inertia (Reynolds) and liquid content within the channel (Martinelli parameter).

Accuracy statistics used for evaluating each correlation are Mean Absolute Error, defined as

Table 2
Annular flow model relations [35].

Mass conservation

$\frac{d\ \dot{m}_f}{d\ z} - \Gamma_{fg} = 0\,;\ \ \frac{d\ \dot{m}_g}{d\ z} + \Gamma_{fg} = 0\,;\ \ \dot{m}_f = \rho_f \int_0^{\delta} u_f\, \pi\ (D-2y)\ \ dy;\ \ \dot{m}_g = \rho_g\, \bar{u}_g\, \pi\ (D-2\ \delta)^2/4\,;\ \ \Gamma_{fg} = q''_w\, \pi\, D/h_{fg}$

Momentum conservation for liquid film

$$\tau = \mu_f \left(1+\frac{\varepsilon_m}{\nu_f}\right)\frac{d\ u_f}{d\ y} = \left(-\frac{d\ p}{d\ z}\right)\frac{A_{f,*}}{P_{f,\,y}} + \frac{\tau_i\, P_{f,\,\delta}+\Gamma_{fg}\, u_i}{P_{f,\,y}} \quad (\textit{Horizontal Flow})$$

$$= \left(-\frac{d\ p}{d\ z} + \rho_f\, g\right)\frac{A_{f,*}}{P_{f,\,y}} + \frac{\tau_i\, P_{f,\,\delta}+\Gamma_{fg}\, u_i}{P_{f,\,y}} \quad (\textit{Vertical Downflow})$$

$$= \left(-\frac{d\ p}{d\ z} - \rho_f\, g\right)\frac{A_{f,*}}{P_{f,\,y}} + \frac{\tau_i\, P_{f,\,\delta}+\Gamma_{fg}\, u_i}{P_{f,\,y}} \quad (\textit{Vertical Upflow})$$

$A_{f,*} = \frac{\pi}{4}(D-2\ y)^2 - \frac{\pi}{4}(D-2\ \delta)^2\,,\ \ P_{f,\,y} = \pi\,(D-2y)\ ,\ \ P_{f,\,\delta} = \pi\,(D-2\ \delta)$

Velocity profile across film

$$u_f(y) = \frac{\delta}{\mu_f}\left(-\frac{dP}{dz}\right)\int_0^{y/\delta}\frac{A_{f,*}}{P_{f,\,y}}\left(1+\frac{\varepsilon_m}{\nu_f}\right)^{-1} d\ \left(\frac{y}{\delta}\right) + \frac{\delta}{\mu_f}\left(\tau_i\ P_{f,\,\delta}+\Gamma_{fg}\ u_i\right)\int_0^{y/\delta}\frac{1}{P_{f,\,y}}\left(1+\frac{\varepsilon_m}{\nu_f}\right)^{-1} d\ \left(\frac{y}{\delta}\right) \quad (\textit{Horizontal Flow})$$

$$= \frac{\delta}{\mu_f}\left(-\frac{dP}{dz} + \rho_f\, g\right)\int_0^{y/\delta}\frac{A_{f,*}}{P_{f,\,y}}\left(1+\frac{\varepsilon_m}{\nu_f}\right)^{-1} d\ \left(\frac{y}{\delta}\right) + \frac{\delta}{\mu_f}\left(\tau_i\ P_{f,\,\delta}+\Gamma_{fg}\ u_i\right)\int_0^{y/\delta}\frac{1}{P_{f,\,y}}\left(1+\frac{\varepsilon_m}{\nu_f}\right)^{-1} d\ \left(\frac{y}{\delta}\right) \quad (\textit{Vertical Downflow})$$

$$= \frac{\delta}{\mu_f}\left(-\frac{dP}{dz} - \rho_f\, g\right)\int_0^{y/\delta}\frac{A_{f,*}}{P_{f,\,y}}\left(1+\frac{\varepsilon_m}{\nu_f}\right)^{-1} d\ \left(\frac{y}{\delta}\right) + \frac{\delta}{\mu_f}\left(\tau_i\ P_{f,\,\delta}+\Gamma_{fg}\ u_i\right)\int_0^{y/\delta}\frac{1}{P_{f,\,y}}\left(1+\frac{\varepsilon_m}{\nu_f}\right)^{-1} d\ \left(\frac{y}{\delta}\right) \quad (\textit{Vertical Upflow})$$

$u_i = u_f(\delta)$

Pressure gradient

$$-\frac{dP}{dz} = \frac{\frac{\mu_f\ \dot{m}_f}{\rho_f\ \delta^2} - \left(\tau_i\ \ P_{f,\,\delta}+\Gamma_{fg}\ u_i\right)\int_0^1\left[P_{f,\,y}\int_0^{y/\delta}\frac{1}{P_{f,\,y}}\left(1+\frac{\varepsilon_m}{\nu_f}\right)^{-1} d\ \left(\frac{y}{\delta}\right)\right] d\ \left(\frac{y}{\delta}\right)}{\int_0^1\left[P_{f,\,y}\int_0^{y/\delta}\frac{A_{f,*}}{P_{f,\,y}}\left(1+\frac{\varepsilon_m}{\nu_f}\right)^{-1} d\ \left(\frac{y}{\delta}\right)\right] d\ \left(\frac{y}{\delta}\right)} \quad (\textit{Horizontal Flow})$$

$$= -\rho_f\, g + \frac{\frac{\mu_f\ \dot{m}_f}{\rho_f\ \delta^2} - \left(\tau_i\ \ P_{f,\,\delta}+\Gamma_{fg}\ u_i\right)\int_0^1\left[P_{f,\,y}\int_0^{y/\delta}\frac{1}{P_{f,\,y}}\left(1+\frac{\varepsilon_m}{\nu_f}\right)^{-1} d\ \left(\frac{y}{\delta}\right)\right] d\ \left(\frac{y}{\delta}\right)}{\int_0^1\left[P_{f,\,y}\int_0^{y/\delta}\frac{A_{f,*}}{P_{f,\,y}}\left(1+\frac{\varepsilon_m}{\nu_f}\right)^{-1} d\ \left(\frac{y}{\delta}\right)\right] d\ \left(\frac{y}{\delta}\right)} \quad (\textit{Vertical Downflow})$$

$$= \rho_f\, g + \frac{\frac{\mu_f\ \dot{m}_f}{\rho_f\ \delta^2} - \left(\tau_i\ \ P_{f,\,\delta}+\Gamma_{fg}\ u_i\right)\int_0^1\left[P_{f,\,y}\int_0^{y/\delta}\frac{1}{P_{f,\,y}}\left(1+\frac{\varepsilon_m}{\nu_f}\right)^{-1} d\ \left(\frac{y}{\delta}\right)\right] d\ \left(\frac{y}{\delta}\right)}{\int_0^1\left[P_{f,\,y}\int_0^{y/\delta}\frac{A_{f,*}}{P_{f,\,y}}\left(1+\frac{\varepsilon_m}{\nu_f}\right)^{-1} d\ \left(\frac{y}{\delta}\right)\right] d\ \left(\frac{y}{\delta}\right)} \quad (\textit{Vertical Upflow})$$

Momentum conservation for vapor core

$$\tau_i = \frac{1}{P_{f,\,\delta}}\left[A_g\left(-\frac{dP}{dz}\right) - \frac{d\ \left(\rho_g\, \bar{u}_g^2\, A_g\right)}{dz} - \Gamma_{fg}\, u_i\right] \quad (\textit{Horizontal Flow})$$

$$= \frac{1}{P_{f,\,\delta}}\left[A_g\left(-\frac{dP}{dz} + \rho_f\, g\right) - \frac{d\ \left(\rho_g\, \bar{u}_g^2\, A_g\right)}{dz} - \Gamma_{fg}\, u_i\right] \quad (\textit{Vertical Downflow})$$

$$= \frac{1}{P_{f,\,\delta}}\left[A_g\left(-\frac{dP}{dz} - \rho_f\, g\right) - \frac{d\ \left(\rho_g\, \bar{u}_g^2\, A_g\right)}{dz} - \Gamma_{fg}\, u_i\right] \quad (\textit{Vertical Upflow})$$

$A_g = \pi\ (D-2\ \delta)^2/4$

Interfacial shear stress relation [83,85]

$\tau_i = \frac{1}{2} f_i\, \rho_g \left(\bar{u}_g - u_i\right)^2 + \frac{\left(u_g - u_i\right)\ \Gamma_{fg}}{2\, P_{f,\,\delta}}$

$f_i = 16/Re_c$ *for* $Re_c < 2{,}000\,;\ f_i = 0.079\, Re_c^{-0.25}$ *for* $2{,}000 \leqslant Re_c < 20{,}000\,,$

$f_i = 0.046\, Re_c^{-0.2}$ *for* $Re_c \geqslant 20{,}000\,;\ \ Re_c = \rho_g \left(\bar{u}_g - u_i\right)(D-2\,\delta)/\mu_g$

Eddy momentum diffusivity [84]

$\frac{\varepsilon_m}{\nu_f} = -\frac{1}{2} + \frac{1}{2}\sqrt{1 + 4K^2\, y^{+2}\left[1-\exp\left(-\sqrt{1-\frac{y^+}{\delta^+}}\,\frac{y^+}{A^+}\right)\right]^2\left(1-\frac{y^+}{\delta^+}\right)^{0.1}\frac{\tau}{\tau_w}}\,;\ \ K = 0.4;\ \ A^+ = 26\left(1+30.18\,\mu_f\,\rho_f^{-0.5}\,\tau_w^{-1.5}\,\frac{dP}{dz}\right)^{-1}$

Turbulent Prandtl number [86]

$\mathrm{Pr}_T = 1.4\,\exp\left(-15\,\frac{y^+}{\delta^+}\right) + 0.66\,;\ \ \ \delta^+ = \delta\, u^*/\nu_f$

Heat transfer coefficient

$$h = \frac{q''_w}{T_{sat}-T_w} = \frac{\rho_f\, c_{p,f}\, u^*}{T_\delta^+} = \frac{\rho_f\, c_{p,f}\, u^*}{\int_0^{\delta^+}\frac{q''}{q''_w}\left(\frac{1}{\mathrm{Pr}_f}+\frac{1}{\mathrm{Pr}_T}\,\frac{\varepsilon_m}{\nu_f}\right)^{-1} d\ y^+} = \frac{\rho_f\, c_{p,f}\, u^*}{\int_0^{\delta^+}\left(\frac{D}{D-2\,\delta}\right)\left(\frac{1}{\mathrm{Pr}_f}+\frac{1}{\mathrm{Pr}_T}\,\frac{\varepsilon_m}{\nu_f}\right)^{-1} d\ y^+}$$

$$MAE = \frac{1}{N}\sum_{n=1}^{N}\left|\frac{h_{pred,n} - h_{\exp,n}}{h_{\exp,n}}\right|, \tag{24}$$

multiplied by 100 and expressed as a percent, as well as θ and ζ, the percent of predictions falling within 30% and 50% of the experimental value, respectively.

Fig. 14(g) indicates that the SFM provides accurate predictions of condensation heat transfer coefficient for the current data set, evidenced by MAE of 31.2%, θ = 41.2%, and ζ = 94.1%. No clear trends with respect to changes in liquid content (X_{tt}) are evident, but predictions clearly become less accurate as Re_{fo} is increased. Before over-analyzing this trend, it should be recalled that Fig. 9(b) indicated vertical downflow condensation results for the highest G_{FC} cases were not entirely water-side independent, and higher water flowrates may lead to slightly lower values of heat transfer coefficient (bring predictions into closer agreement with experimental values). It is expected altering the test matrix to include higher G_{H2O} cases for the ISS experiment will allow this to be tested.

5.2. Common correlations for horizontal flow

While the Separated Flow Model provided the most accurate predictions of vertical downflow condensation for the current dataset, common semi-empirical correlations were found to give sufficiently accurate predictions for horizontal flow. Several of these are evaluated here, and suggestions made on which should be used for similar applications.

Similar to that done by Kim and Mudawar in their review [87], correlations used here have been split into those intended for use with macro-channels and those for mini/micro-channels (indicating prevalence of confinement effects). Macro-channel correlations include those by Akers and Rosson [88], Cavallini and Zecchin [89], Shah [90], Haraguchi et al. [91], Dobson and Chato [33], Moser et al. [92], and the updated Shah correlation [94]. Mini/micro-channel correlations include those by Wang et al. [95], Koyama et al. [96], Huang et al. [97], Bohdal et al. [98], Park et al. [99], and Kim and Mudawar [73]. Full forms of all correlations are provided in Table 3,

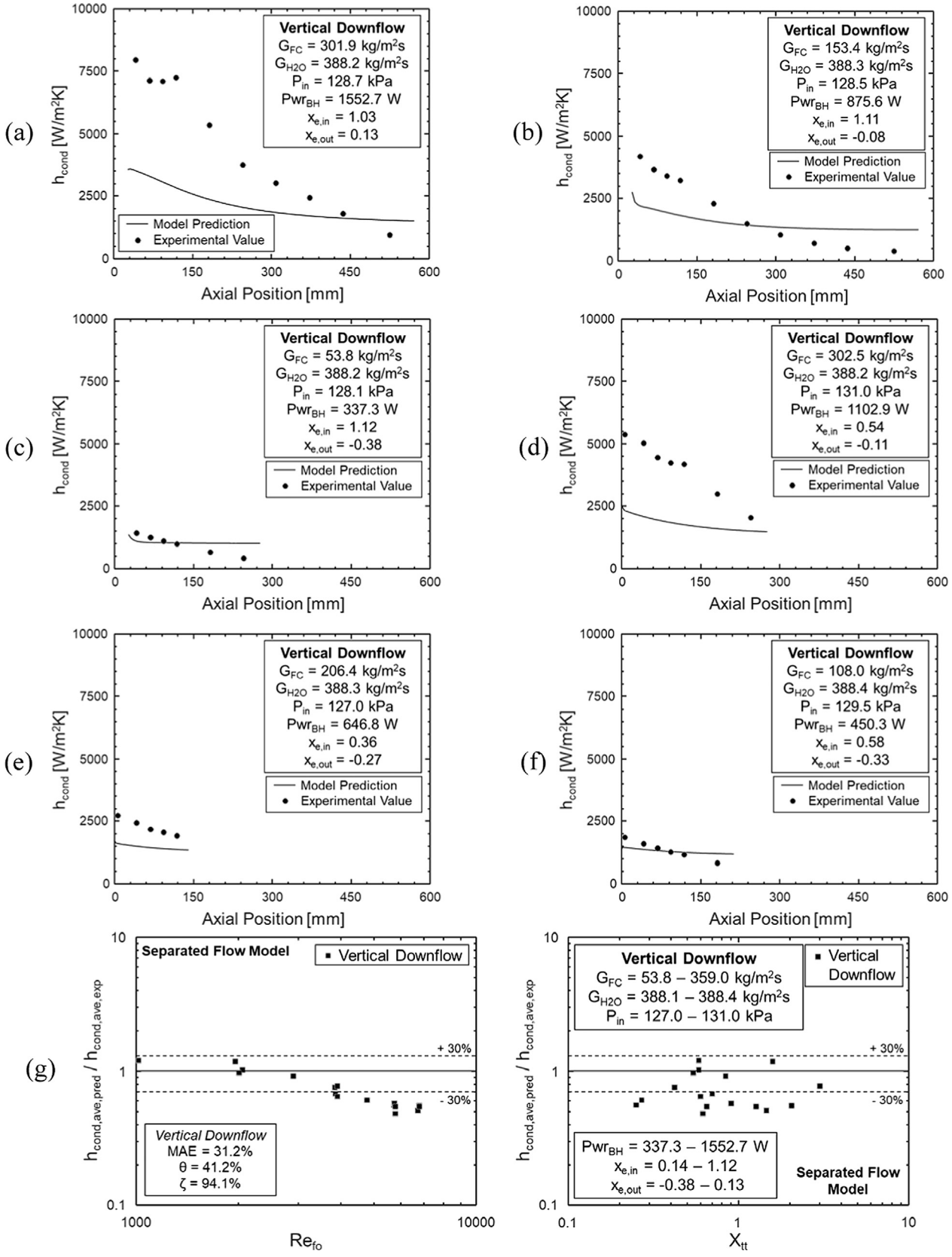

Fig. 14. Separated flow model local heat transfer predictions for vertical downflow with (a), (b), (c) superheated vapor inlet and descending mass velocity, (d), (e), (f) two-phase inlet and descending mass velocity, and (g) overall performance of SFM channel-average heat transfer predictions.

Table 3
Condensation heat transfer coefficient correlations evaluated.

Author(s)	Equation	Remarks	MAE (%) *Horizontal*	θ (%) *Horizontal*	ζ (%) *Horizontal*
Recommended for macro-channels					
Akers and Rosson [88]	$\frac{h_{tp}D_h}{k_f} = 0.026Pr_f^{1/3}\left\{G\left[(1-x)+x\left(\frac{\rho_f}{\rho_g}\right)^{0.5}\right]\frac{D_h}{\mu_f}\right\}^{0.8}$	D = 19.05 mm R12, propane $Re_g\left(\frac{\mu_g}{\mu_f}\right)\left(\frac{\rho_f}{\rho_g}\right)^{0.5} > 20,000$ $Re_f > 5000$	61.3	0	7.1
Cavallini and Zecchin [89]	$\frac{h_{tp}D_h}{k_f} = 0.05Re_f^{0.8}Pr_f^{0.33}\left[1+\left(\frac{\rho_f}{\rho_g}\right)^{0.5}\left(\frac{x}{1-x}\right)\right]^{0.8}$	R12, R22, R113 $7000 \leqslant Re_{fo} \leqslant 53,000$	26.1	64.3	92.9
Shah (1979) [90]	$\frac{h_{tp}D_h}{k_f} = 0.023Re_{fo}^{0.8}Pr_f^{0.4}\left[(1-x)^{0.8}+\frac{3.8x^{0.76}(1-x)^{0.04}}{P_R^{0.38}}\right]$	D = 7–40 mm Water, R11, R12, R22, R113, methanol, ethanol, benzene, toluene, trichloroethylene	34.1	35.7	85.7
Haraguchi et al. [91]	$\frac{h_{tp}D_h}{k_f} = 0.0152Re_f^{0.77}\frac{\phi_g}{X_{tt}}\left(1+0.6\mathrm{Pr}_f^{0.8}\right)$ $X_{tt} = \left(\frac{\mu_f}{\mu_g}\right)^{0.1}\left(\frac{1-x}{x}\right)^{0.9}\left(\frac{v_f}{v_g}\right)^{0.5}$ $\phi_g = 1+0.5\left[\frac{G}{\sqrt{g\rho_g(\rho_f-\rho_g)D_h}}\right]^{0.75}X_{tt}^{0.35}$	D = 8.4 mm R22, R123, R134a	36.2	42.9	78.6
Dobson and Chato [33]	$\frac{h_{tp}D_h}{k_f} = 0.023Re_f^{0.8}Pr_f^{0.4}\left(1+\frac{2.22}{X_{tt}^{0.89}}\right)$	D = 3.14–7.04 mm R12, R22, R134a, R32/R125	24.1	71.4	100
Moser et al. [92] (Friedel [93])	$\frac{h_{tp}D_h}{k_f} = \frac{0.0994^{C_1}Re_f^{C_2}Re_{eq}^{1+0.875C_1}Pr_f^{0.815}}{\left[1.58\ln(Re_{eq})-3.28\right]\left[2.58\ln(Re_{eq})+13.7Pr_f^{2/3}-19.1\right]}$ $C_1 = 0.126Pr_f^{-0.448}$ $C_2 = -0.113Pr_f^{-0.563}$ $Re_{eq} = \phi_{fo,Friedel}^{8/7}Re_{fo}$	D = 3.14–20 mm R11, R12, R125, R22, R134a, R410a	39.5	21.4	78.6
Shah (2009) [94]	$j_g = \frac{xG}{\sqrt{gD\rho_g(\rho_f-\rho_g)}}$, $Z_{Shah} = \left(\frac{1}{x}-1\right)^{0.8}P_R^{0.4}$ For Vertical and Inclined Tubes: if $j_g \geqslant \frac{1}{2.4Z_{shah}+0.73}$: $\frac{h_{tp}D_h}{k_f} = 0.023Re_{fo}^{0.8}Pr_f^{0.4}\left(\frac{\mu_f}{14\mu_g}\right)^n\left[(1-x)^{0.8}+\frac{3.8x^{0.76}(1-x)^{0.04}}{P_R^{0.38}}\right]$ where $n = 0.0058+0.557P_R$ elseif $j_g \leqslant 0.89-0.93\exp\left(-0.087Z_{Shah}^{-1.17}\right)$: $\frac{h_{tp}D_h}{k_f} = 1.32\frac{D_h}{k_f}Re_f^{-1/3}\left[\frac{\rho_f(\rho_f-\rho_g)gk_f^3}{\mu_f^2}\right]^{1/3}$ else : $\frac{h_{tp}D_h}{k_f} = 0.023Re_{fo}^{0.8}Pr_f^{0.4}\left(\frac{\mu_f}{14\mu_g}\right)^n\left[(1-x)^{0.8}+\frac{3.8x^{0.76}(1-x)^{0.04}}{P_R^{0.38}}\right]$ $+1.32\frac{D_h}{k_f}Re_f^{-1/3}\left[\frac{\rho_f(\rho_f-\rho_g)gk_f^3}{\mu_f^2}\right]^{1/3}$ For Horizontal Tubes: if $j_g \geqslant 0.98(Z_{Shah}+0.263)^{-0.62}$: $\frac{h_{tp}D_h}{k_f} = 0.023Re_{fo}^{0.8}Pr_f^{0.4}\left(\frac{\mu_f}{14\mu_g}\right)^n\left[(1-x)^{0.8}+\frac{3.8x^{0.76}(1-x)^{0.04}}{P_R^{0.38}}\right]$ where $n = 0.0058+0.557P_R$ else : $\frac{h_{tp}D_h}{k_f} = 0.023Re_{fo}^{0.8}Pr_f^{0.4}\left(\frac{\mu_f}{14\mu_g}\right)^n\left[(1-x)^{0.8}+\frac{3.8x^{0.76}(1-x)^{0.04}}{P_R^{0.38}}\right]$ $+1.32\frac{D_h}{k_f}Re_f^{-1/3}\left[\frac{\rho_f(\rho_f-\rho_g)gk_f^3}{\mu_f^2}\right]^{1/3}$	D_h = 2–49 mm Water, R11, R12, R22, R113, R123, R134a, benzene, R32, R125, R404A, R410A, R507, propylene, propane, isobutane, R142b, R502, methanol, ethanol, toluene, Dowtherm 209.	24.7	57.1	100
Recommended for mini/micro-channels					
Wang et al. [95]	$\frac{h_{tp}D_h}{k_f} = 0.0274Re_f^{0.6792}Pr_f x^{0.2208}\frac{\phi_g}{X_{tt}}$ $\phi_g^2 = 1.376+8X_{tt}^{1.665}$	D_h = 1.46 mm, Multi-channel R134a	24.2	64.3	100
Koyama et al. [96]	$\frac{h_{tp}D_h}{k_f} = 0.0152\left(1+0.6Pr_f^{0.8}\right)Re_f^{0.77}\frac{\phi_g}{X_{tt}}$ $\phi_g^2 = 1+21[1-\exp(-0.319D_h)]X_{tt}+X_{tt}^2$	D_h = 0.80 and 1.11 mm, Multi-channel R134a	62.0	0	7.1
Huang et al. [97]	$\frac{h_{tp}D_h}{k_f} = 0.0152\left(-0.33+0.83Pr_f^{0.8}\right)Re_f^{0.77}\frac{\phi_g}{X_{tt}}$ $\phi_g = \phi_{g,Haraguchi}$	D = 1.6 and 4.18 mm R410A, R410A/oil	38.8	35.7	78.6
Bohdal et al. [98]	$\frac{h_{tp}D_h}{k_f} = 25.084Re_f^{0.258}Pr_f^{-0.495}P_R^{-0.288}\left(\frac{x}{1-x}\right)^{0.266}$	D = 0.31–3.30 mm R134a, R404a	58.5	0	21.4
Park et al. [99]	$\frac{h_{tp}D_h}{k_f} = 0.0055Pr_f^{1.37}Re_f^{0.7}\frac{\phi_g}{X_{tt}}$ $\phi_g^2 = 1+13.17\left(\frac{\rho_g}{\rho_f}\right)^{0.17}\left[1-\exp\left(-0.6\sqrt{\frac{g(\rho_f-\rho_g)D_h^2}{\sigma}}\right)\right]X_{tt}+X_{tt}^2$	D_h = 1.45 mm, Multi-channel R134a, R236fa, R1234ze(E)	53.4	0	35.7
Kim and Mudawar [73]	for $We^* > 7X_{tt}^{0.2}$: $\frac{h_{tp}D_h}{k_f} = 0.048Re_f^{0.69}Pr_f^{0.34}\frac{\phi_g}{X_{tt}}$ for $We^* \leqslant 7X_{tt}^{0.2}$: $\frac{h_{tp}D_h}{k_f} = \left[\left(0.048Re_f^{0.69}Pr_f^{0.34}\frac{\phi_g}{X_{tt}}\right)^2+\left(3.2\times10^{-7}Re_f^{-0.38}Su_{go}^{1.39}\right)^2\right]^{0.5}$	D_h = 0.424–6.22 mm R12, R123, R1234yf, R1234ze (E), R134a, R22, R236fa, R245fa, R32, R404A, R410A, R600a, FC72, methane, CO_2	39.5	21.4	85.7

(*continued on next page*)

Table 3 (*continued*)

Author(s)	Equation	Remarks	MAE (%) *Horizontal*	θ (%) *Horizontal*	ζ (%) *Horizontal*
	where $X_{tt} = \left(\frac{\mu_f}{\mu_g}\right)^{0.1}\left(\frac{1-x}{x}\right)^{0.9}\left(\frac{\rho_g}{\rho_f}\right)^{0.5}$ $\phi_g^2 = 1 + CX + X^2, X^2 = \frac{(dP/dz)_f}{(dP/dz)_g}$ $-\left(\frac{dP}{dz}\right)_f = \frac{2f_f v_f G^2(1-x)^2}{D_h}$, $-\left(\frac{dP}{dz}\right)_g = \frac{2f_g v_g G^2 x^2}{D_h}$ $f_k = 16Re_k^{-1}$ for $Re_k < 2000$ $f_k = 0.079Re_k^{-0.25}$ for $2000 \leqslant Re_k < 20,000$ $f_k = 0.046Re_k^{-0.2}$ for $Re_k \geqslant 20,000$ where subscript k denotes f or g for liquid or vapor phases, respectively				
	$Re_f \geqslant 2000,\ Re_g \geqslant 2000$ (tt); $C = 0.39Re_{fo}^{0.03}Su_{go}^{0.10}\left(\frac{\rho_f}{\rho_g}\right)^{0.35}$				
	$Re_f \geqslant 2000,\ Re_g < 2000$ (tv); $C = 8.7 \times 10^{-4}Re_{fo}^{0.17}Su_{go}^{0.50}\left(\frac{\rho_f}{\rho_g}\right)^{0.14}$				
	$Re_f < 2000,\ Re_g \geqslant 2000$ (vt); $C = 0.0015Re_{fo}^{0.59}Su_{go}^{0.19}\left(\frac{\rho_f}{\rho_g}\right)^{0.36}$				
	$Re_f < 2000,\ Re_g < 2000$ (vv); $C = 3.5 \times 10^{-5}Re_{fo}^{0.44}Su_{go}^{0.50}\left(\frac{\rho_f}{\rho_g}\right)^{0.48}$				

along with information on the experimental work and performance evaluated using the current dataset.

Similar to Fig. 14(g), Fig. 15 provides plots of the ratio of predicted to experimental heat transfer coefficient versus Re_{fo} and X_{tt}. Fig. 15(a), providing results for the correlation of Akers and Rosson [88], indicates the correlation under-predicts experimental heat transfer values for all operating conditions tested here.

Fig. 15(b) shows results are much better using the correlation of Cavallini and Zecchin [89], with horizontal flow exhibiting MAE of 26.1%. Their correlation appears to predict results with higher accuracy for high flow inertia and low liquid content cases.

Fig. 15(c) presents similar results for the original Shah correlation [90]. Cases with low liquid content (low values of X_{tt}) again yield more accurate predictions.

These trends continue to manifest in Fig. 15(d), which shows the correlation of Haraguchi et al. [91] performing significantly better for high flowrates and low liquid content within the channel.

The correlation of Dobson and Chato [33], shown in Fig. 15(e), remains relatively accurate for all flowrates tested in the current dataset, but again struggles to accurately predict results in cases with low flow quality (high X_{tt}). Similar results are seen for both the correlations of Moser et al. [92] and the modified Shah correlation [94], shown in Fig. 15(f) and (g), respectively.

Fig. 16 provides similar results using correlations intended for mini/micro-channel flows. Fig. 16(a), corresponding to the correlation of Wang et al. [95], offers one of the highest predictive accuracy of any correlation tested here with MAE of 24.2%. Predictive accuracy is similar for all flowrates tested but decreases slightly for higher liquid content.

Fig. 16(b) shows the correlation of Koyama et al. [98] underpredicting results for all cases tested here. The correlation of Huang et al. [97], shown in Fig. 16 (c), underpredicts heat transfer coefficient for low flowrates and high liquid content, but offers reasonable predictions for high flowrates and low liquid content within the channel.

Fig. 16(d) and (e) both significantly under predict results for all operating conditions investigated here. Fig. 16(d), corresponding to the correlation of Bohdal et al. [98], seems to offer better predictions for lower ranges of Reynolds number, dissimilar to what is seen for most correlations investigated here.

Finally, Fig. 16(f) provides results from the universal correlation developed by Kim and Mudawar [73]. Their correlation offers reasonable predictive results for all flowrates tested, but underpredicts condensation heat transfer coefficient for higher liquid content cases.

Across all correlations investigated here several key trends may be seen:

(1) The correlations of Shah [94], Wang et al. [95], and Dobson and Chato [33] offer the greatest predictive accuracy for the current dataset, with MAEs of 24.7%, 24.2%, and 24.1%, respectively.
(2) Most correlations predict results with higher accuracy for high flowrate cases.
(3) Almost every correlation struggles to accurately predict condensation heat transfer for low flow qualities (high liquid content). It is likely that most correlations shown here do not perform well due to an absence of low-quality datapoints for the datasets used in their original formulation.

5.3. Challenges with predicting vertical upflow

Due to the role of body force destabilizing flow in vertical upflow condensation [71,74], this orientation is far less frequently adopted than vertical downflow and horizontal configurations. Difficulty in establishing co-current flow found in other orientations leads to significantly different heat transfer mechanisms in vertical upflow condensation, meaning many common semi-empirical and mechanistic design tools struggle to accurately capture heat transfer behavior in vertical upflow condensation, particularly in cases with high liquid content and low flow inertia.

Because of these limitations in predictive tools and the rare nature of condensers operating in vertical upflow orientation, the current experimental results will not be compared to any commonly available predictive tools. Should design of a condenser in vertical upflow orientation be necessary, adoption of a micro-channel heat sink is recommended, as these are less susceptible to orientation effects (due to the dominant role of surface tension) and have many associated predictive tools which may be used with higher accuracy.

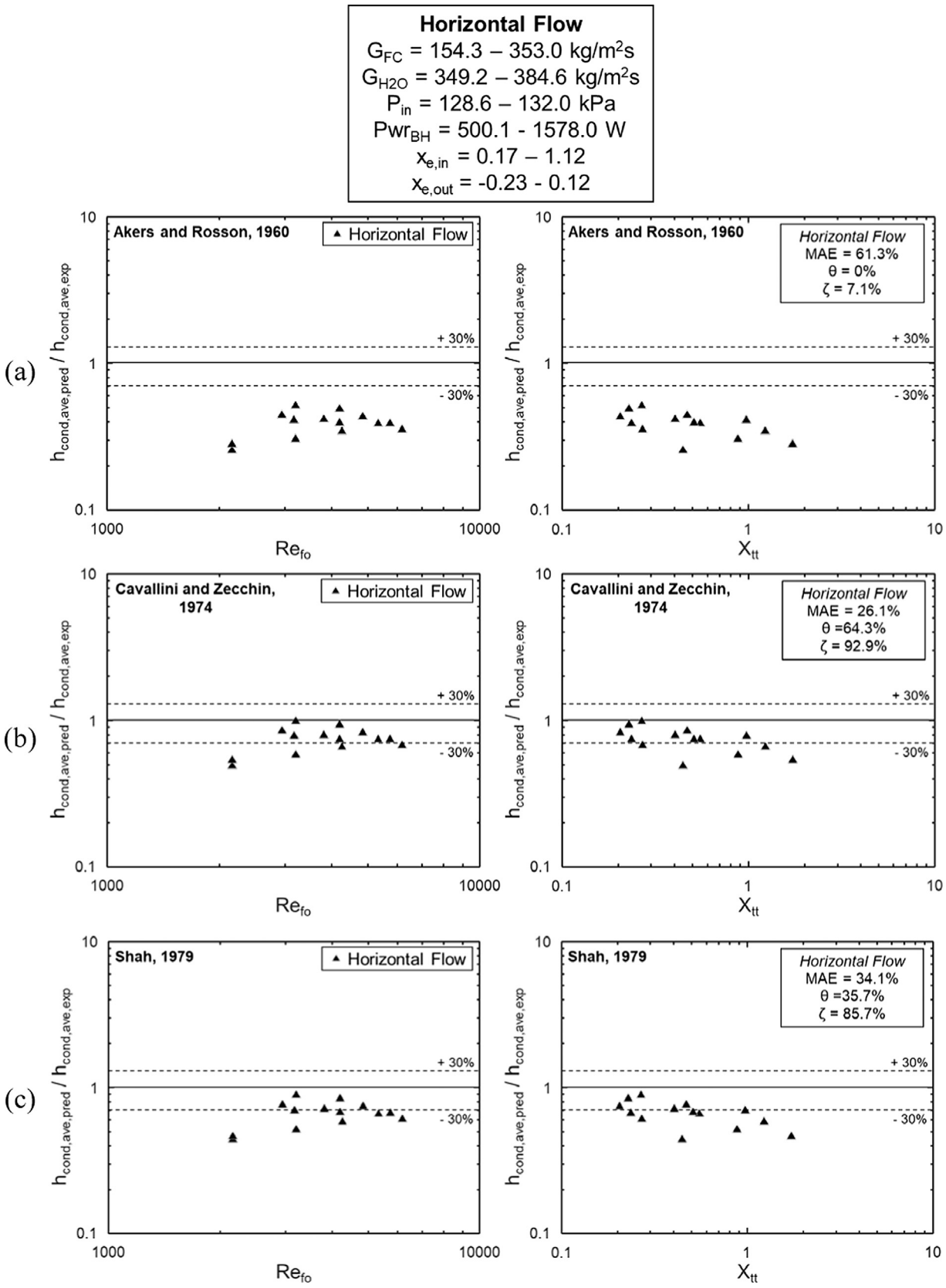

Fig. 15. Ratio of experimental to predicted heat channel average heat transfer coefficient versus liquid-only Reynolds number and X_{tt}, with heat transfer coefficient values predicted by correlations of (a) Akers and Rosson [88], (b) Cavallini and Zecchin [89], (c) Shah [90], (d) Haraguchi et al. [91], (e) Dobson and Chato [33], (f) Moser et al. [92], and (g) the updated Shah correlation [94]. Correlations shown here are recommended for use with macro-channels.

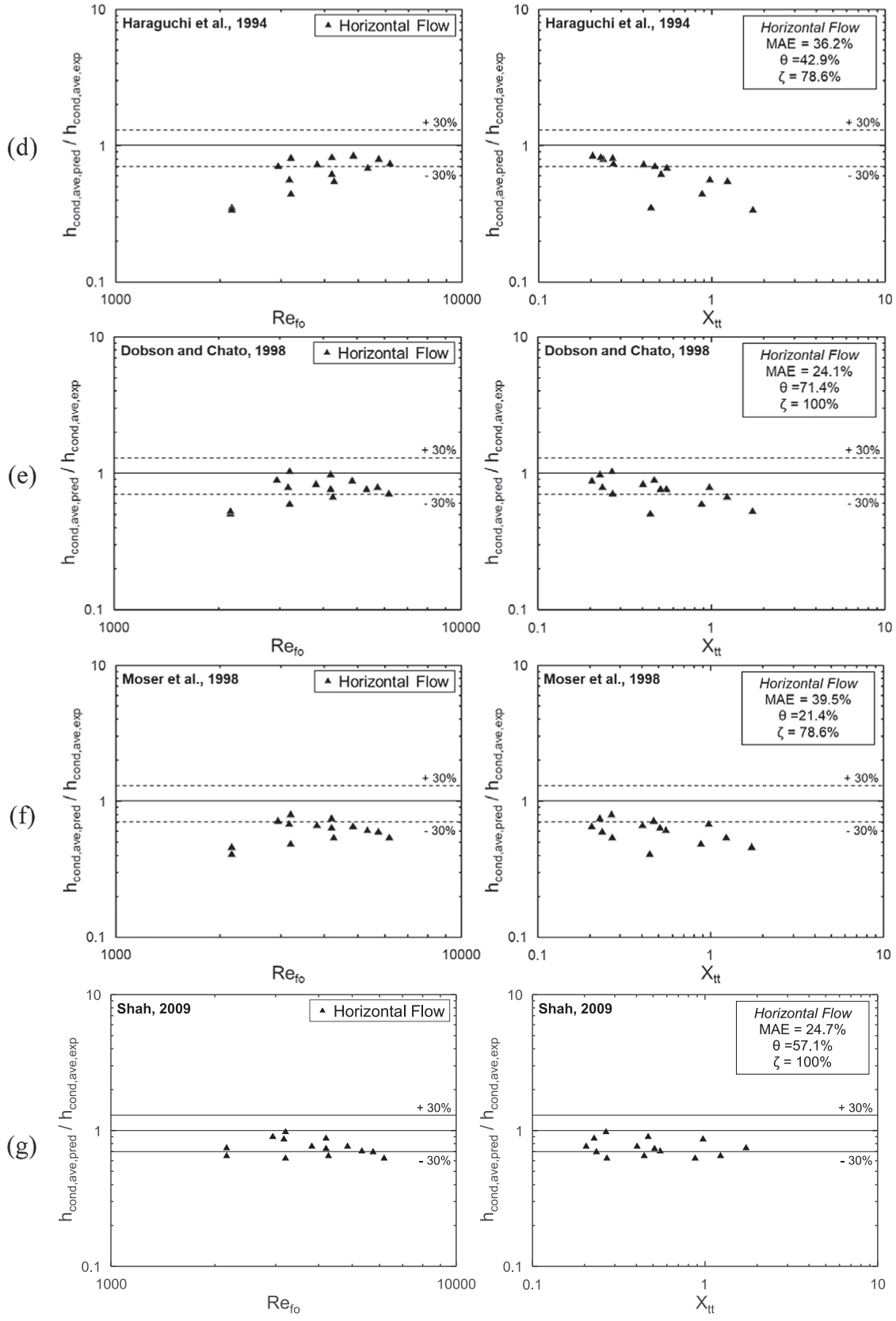

Fig. 15 (*continued*)

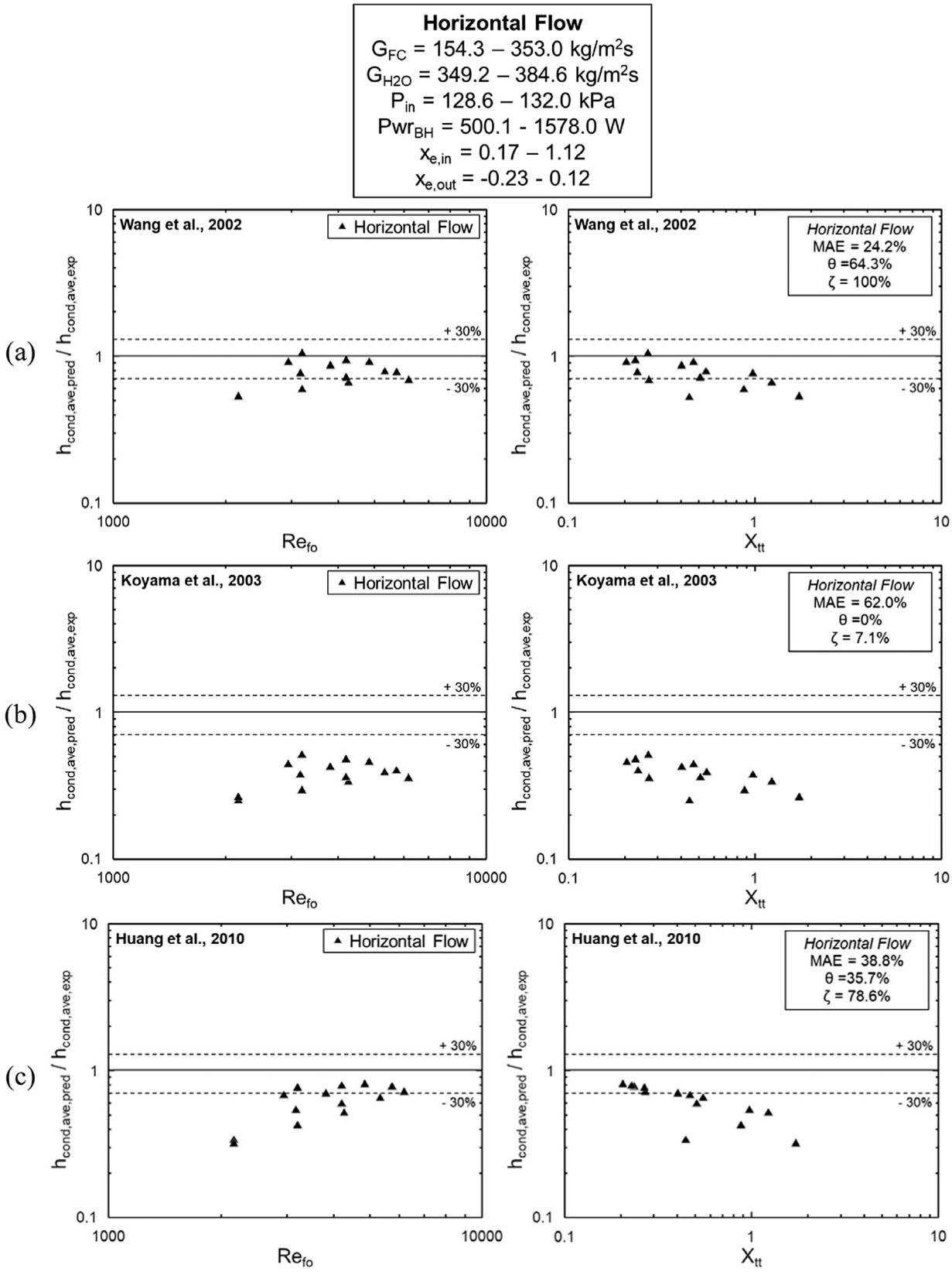

Fig. 16. Ratio of experimental to predicted heat channel average heat transfer coefficient versus liquid-only Reynolds number and X_{tt}, with heat transfer coefficient values predicted by correlations of (a) Wang et al. [95], (b) Koyama et al. [96], (c) Huang et al. [97], (d) Bohdal et al. [98], (e) Park et al. [99], and (f) Kim and Mudawar [73]. Correlations shown here are recommended for use with mini/micro-channels.

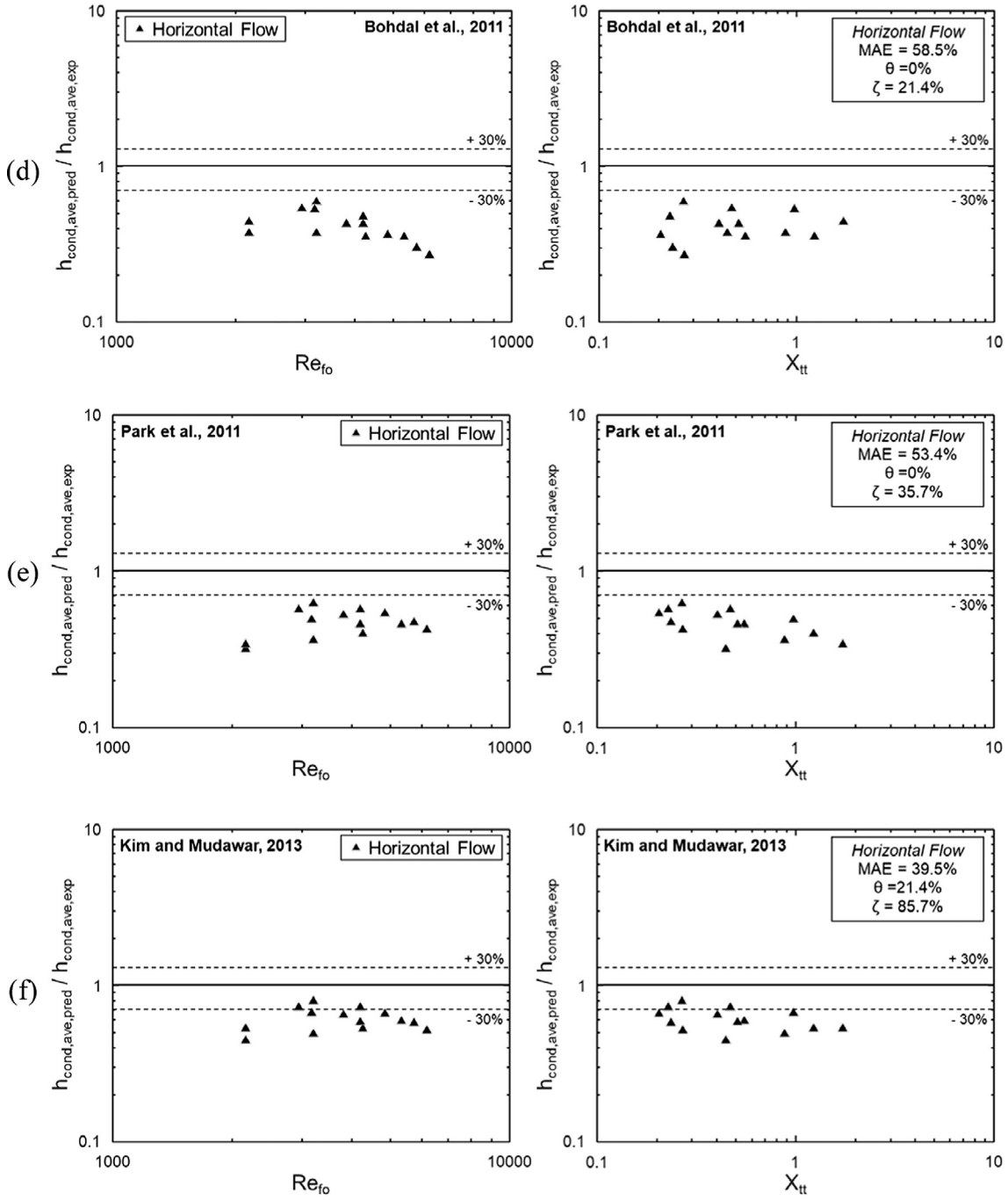

Fig. 16 (*continued*)

6. Conclusions

The present study dealt with flow condensation of dielectric FC-72 in a smooth circular tube at different orientations in Earth's gravity. Calculation of both local and channel average condensation heat transfer coefficient values was performed for a subset of the dataset corresponding to axisymmetric flow conditions. Uncertainty analysis was also presented for calculated values of condensation heat transfer coefficient, showing channel average values possess low uncertainty (~5–25%), but local measurements near the channel outlet may possess high uncertainties (~25–100%).

Parametric analysis of both local and averaged condensation heat transfer coefficient values reveal mass velocity is the dominant parameter governing changes in heat transfer coefficient value (increases in mass velocity yield increased heat transfer coefficient assuming all other operating conditions are held constant). Flow quality also influences heat transfer coefficient, with higher liquid content (lower quality) leading to lower values of condensation heat transfer coefficient.

Channel orientation was also seen to influence condensation heat transfer, particularly at low mass velocities. At low mass velocities vertical upflow is seen to exhibit highest values of heat transfer coefficient, while as mass velocity is increased results for all three orientations begin to converge. Gravity independence criteria developed by O'Neill et al. [62] are evaluated using the present dataset and are seen to give reasonable estimation of gravity independence point.

Comparison of experimental heat transfer results in vertical downflow orientation with SFM predictions yielded good agreement, particularly for low mass velocity cases. For horizontal flow, evaluation of correlations commonly found in literature revealed the majority of correlations slightly under predict heat transfer in the current dataset, and particularly struggle with low flow quality cases. The correlations of Shah [94], Wang et al. [95], and Dobson and Chato [33] were seen to offer the best predictive performance across all three orientations.

Key conclusions from this study are:

(1) Identification of condensation flow regime using temperature and pressure based methods presented in the companion study [74] prior to heat transfer data reduction is crucial for eliminating non-axisymmetric cases from the dataset and identifying countercurrent flow cases for later analysis.
(2) Uncertainty analysis for heat transfer coefficient calculations revealed channel average heat transfer coefficient values are calculated with uncertainties of ±3.6% to ±26.7% (depending on operating conditions). Local heat transfer coefficient values in the channel exit region may have significantly higher uncertainties, however, and trends for this portion of the channel should be analyzed with caution.
(3) Mass velocity is seen to be the dominant parameter governing changes in condensation heat transfer coefficient. Liquid content plays a secondary role, and orientation (body force) is also seen to have an influence, particularly at low flowrates.
(4) Separated Flow Model (outlined in Table 2) predictions for vertical downflow condensation heat transfer yield reasonable agreement with experimental results, evidenced by an overall MAE of 31.2% on the current dataset.
(5) Assessment of correlations for heat transfer coefficient in horizontal flow reveal the majority do a reasonable job of predicting heat transfer coefficient. Most correlations struggle to predict heat transfer in cases with high liquid content (low quality) and the majority of inaccuracies come from these cases. Best predictive results are found for the correlations of Shah [94], Wang et al. [95], and Dobson and Chato [33], with MAEs of 24.7%, 24.2%, and 24.1%, respectively.

Future experiments on the International Space Station (ISS) involving tests at similar operating conditions using a test section with the same diameter and condensation length will provide a microgravity dataset for comparison with the current 1-g results. It is expected these results will greatly further understanding of the role of body force on the condensation heat transfer process.

Declaration of Competing Interest

The authors declared that there is no conflict of interest.

Acknowledgement

The authors are grateful for financial support provided by the National Aeronautics and Space Administration (NASA) under grant no. NNX17AK98G, and technical support of the NASA Glenn Research Center, Cleveland, Ohio. This work was also supported by NASA Space Technology Research Fellowship NNX15AP29H.

Appendix A. Supplementary material

Supplementary data to this article can be found online at https://doi.org/10.1016/j.ijheatmasstransfer.2019.05.103.

References

[1] I. Mudawar, Assessment of high-heat-flux thermal management schemes, IEEE Trans. - CPMT 24 (2001) 122–141.
[2] S. Lee, I. Mudawar, M.M. Hasan, Thermal analysis of hybrid single-phase, two-phase and heat pump thermal control system (TCS) for future spacecraft, Appl. Therm. Eng. 100 (2016) 190–214.
[3] F.P. Chiramonte, J.A. Joshi, Workshop on critical issues in microgravity fluids, transport, and reaction processes in advanced human support technology – final report, NASA TM-2004-212940, 2004.
[4] The national Academies, Recapturing a Future for Space Exploration: Life and Physical Sciences Research for a New Era, National Academies Press, Washington, DC, 2011.
[5] P.J. Marto, V.J. Lepere, Pool boiling heat transfer from enhanced surfaces to dielectric fluids, J. Heat Transfer 104 (1982) 292–299.
[6] I. Mudawar, T.M. Anderson, Parametric investigation into the effects of pressure, subcooling, surface augmentation and choice of coolant on pool boiling in the design of cooling systems for high-power density chips, J. Electronic Packag. 112 (1990) 375–382.
[7] D.E. Maddox, I. Mudawar, Single- and two-phase convective heat transfer from smooth and enhanced microelectronic heat sources in a rectangular channel, J. Heat Transfer 111 (1989) 533–542.
[8] I. Mudawar, D.E. Maddox, Enhancement of critical heat flux from high power microelectronic heat sources in a flow channel, J. Electronic Packag. 112 (1990) 241–248.
[9] C.O. Gersey, I. Mudawar, Effects of heater length and orientation on the trigger mechanism for near-saturated flow boiling critical heat flux – I. Photographic study and statistical characterization of the near-wall interfacial features, Int. J. Heat Mass Transfer 38 (1995) 629–641.
[10] J.C. Sturgis, I. Mudawar, Critical heat flux in a long, rectangular channel subjected to one-sided heating – I. Flow visualization, Int. J. Heat Mass Transfer 42 (1999) 1835–1847.
[11] J.C. Sturgis, I. Mudawar, Critical heat flux in a long, rectangular channel subjected to one-sided heating – II. Analysis of critical heat flux data, Int. J. Heat Mass Transfer 42 (1999) 1849–1862.
[12] S.M. Ghiaasiaan, Two-Phase Flow, Boiling and Condensation in Conventional and Miniature Systems, Cambridge University Press, New York, 2008.
[13] D.D. Hall, I. Mudawar, Ultra-high critical heat flux (CHF) for subcooled water flow boiling – II: high-CHF database and design equations, Int. J. Heat Mass Transfer 42 (1999) 1429–1456.
[14] T.J. LaClair, I. Mudawar, Thermal transients in a capillary evaporator prior to the initiation of boiling, Int. J. Heat Mass Transfer 43 (2000) 3937–3952.
[15] S. Mukherjee, I. Mudawar, Smart pumpless loop for micro-channel electronic cooling using flat and enhanced surfaces, IEEE Trans. – CPMT 26 (2003) 99–109.
[16] W. Qu, I. Mudawar, Thermal design methodology for high-heat-flux single-phase and two-phase micro-channel heat sinks, in: Proc. I-THERM 2002, San Diego, California, pp. 347–359.
[17] S. Mukherjee, I. Mudawar, Pumpless loop for narrow channel and micro-channel boiling from vertical surfaces, J. Electronic Packag. 125 (2003) 431–441.
[18] W. Qu, I. Mudawar, S.Y. Lee, S.T. Wereley, Experimental and computational investigation of flow development and pressure drop in a rectangular micro-channel, J. Electronic Packag. 128 (2005) 1–9.
[19] J. Lee, I. Mudawar, Critical heat flux for subcooled flow boiling in micro-channel heat sinks, Int. J. Heat Mass Transfer 52 (2009) 3341–3352.
[20] D.C. Wadsworth, I. Mudawar, Enhancement of single-phase heat transfer and critical heat flux from an ultra-high-flux simulated microelectronic heat source to a rectangular impinging jet of dielectric liquid, J. Heat Transfer 114 (1992) 764–768.
[21] M.E. Johns, I. Mudawar, An ultra-high power two-phase jet-impingement avionic clamshell module, J. Electronic Packag. 118 (1996) 264–270.
[22] W.P. Klinzing, J.C. Rozzi, I. Mudawar, Film and transition boiling correlations for quenching of hot surfaces with water sprays, J. Heat Treat. 9 (1992) 91–103.
[23] D.D. Hall, I. Mudawar, Experimental and numerical study of quenching complex-shaped metallic alloys with multiple, overlapping sprays, Int. J. Heat Mass Transfer 38 (1995) 1201–1216.
[24] L. Lin, R. Ponnappan, Heat transfer characteristics of spray cooling in a closed loop, Int. J. Heat Mass Transfer 46 (2003) 3737–3746.
[25] M. Visaria, I. Mudawar, Effects of high subcooling on two-phase spray cooling and critical heat flux, Int. J. Heat Mass Transfer 51 (2008) 5269–5278.
[26] M. Visaria, I. Mudawar, Application of two-phase spray cooling for thermal management of electronic devices, IEEE Trans. – CPMT 32 (2009) 784–793.
[27] M.K. Sung, I. Mudawar, Single-phase hybrid micro-channel/jet impingement cooling, Int. J. Heat Mass Transfer 51 (2008) 4342–4352.
[28] M.M. Chen, An analytical study of laminar film condensation: Part 2 - Single and multiple horizontal tubes, J. Heat Transfer 83 (1961) 55–60.
[29] J.F. Roques, V. Dupont, J.R. Thome, Falling film transitions on plain and enhanced tubes, J. Heat Transfer 124 (2002) 491–499.
[30] Y.T. Kang, H. Hong, Y.S. Lee, Experimental correlation of falling film condensation on enhanced tubes with HFC134a; low-fin and Turbo-C tubes, Int. J. Refrig. 30 (2007) 805–811.
[31] M. Soliman, J.R. Schuster, P.J. Berenson, A general heat transfer correlation for annular flow condensation, J. Heat Transfer 90 (1968) 267–274.

[32] G. Breber, J.W. Palen, J. Taborek, Prediction of horizontal tubeside condensation of pure components using flow regime criteria, J. Heat Transfer 102 (1980) 471–476.
[33] M.K. Dobson, J.C. Chato, Condensation in smooth horizontal tubes, J. Heat Transfer 120 (1998) 193–213.
[34] D. Jung, K. Song, Y. Cho, S. Kim, Flow condensation heat transfer coefficients of pure refrigerants, Int. J. Refrig. 26 (2003) 4–11.
[35] I. Park, S.M. Kim, I. Mudawar, Experimental measurement and modeling of downflow condensation in a circular tube, Int. J. Heat Mass Transfer 57 (2013) 567–581.
[36] I. Park, I. Mudawar, Climbing film, flooding and falling film behavior in upflow condensation in tubes, Int. J. Heat Mass Transfer 65 (2013) 44–61.
[37] I. Park, H. Lee, I. Mudawar, Determination of flow regimes and heat transfer coefficient for condensation in horizontal tubes, Int. J. Heat Mass Transfer 80 (2015) 688–716.
[38] X.R. Zhuang, G.F. Chen, H. Guo, Q.L. Song, Q.X. Tang, Z.Q. Yang, X. Zou, M.Q. Gong, Experimental investigation on flow condensation of zeotropic mixtures of methane/ethane in a horizontal smooth tube, Int. J. Refrig. 85 (2018) 120–134.
[39] X. Quan, P. Cheng, H. Wu, Transition from annular flow to plug/slug flow in condensation of steam in microchannels, Int. J. Heat Mass Transfer 51 (2008) 707–716.
[40] S.M. Kim, J. Kim, I. Mudawar, Flow condensation in parallel micro-channels - Part 1: experimental results and assessment of pressure drop correlations, Int. J. Heat Mass Transfer 55 (2012) 971–983.
[41] S.M. Kim, I. Mudawar, Flow condensation in parallel micro-channels - Part 2: heat transfer results and correlation technique, Int. J. Heat Mass Transfer 55 (2012) 984–994.
[42] G. Liang, N. Mascarenhas, I. Mudawar, Analytical and experimental determination of slug flow parameters, pressure drop and heat transfer coefficient in micro-channel condensation, Int. J. Heat Mass Transfer 111 (2017) 1218–1233.
[43] M.A. Vanderputten, T.A. Jacob, M. Sattar, N. Ali, B.M. Fronk, Two-phase flow regimes of condensing R-134a at low mass flux in rectangular microchannels, Int. J. Refrig. 84 (2017) 92–102.
[44] J. Wang, J.M. Li, Theoretical and experimental study of wavy flow during R134a condensation flow in symmetrically and asymmetrically cooled microchannels, Int. J. Multiphase Flow 101 (2018) 125–136.
[45] A. Umur, P. Griffith, Mechanism of dropwise condensation, J. Heat Transfer 87 (1965) 275–282.
[46] J.W. Rose, L.R. Glicksman, Dropwise condensation - The distribution of drop sizes, Int. J. Heat Mass Transfer 16 (1973) 411–425.
[47] X. Chen, M.M. Derby, Droplet departure modeling and a heat transfer correlation for dropwise flow condensation in hydrophobic min-channels, Int. J. Heat Mass Transfer 125 (2018) 1096–1104.
[48] Y. Chen, C.B. Sobhan, G.P. Peterson, Review of condensation heat transfer in microgravity environments, J. Therm. Heat Transfer 3 (2006) 353–360.
[49] S. Lips, J.P. Meyer, Two-phase flow in inclined tubes with specific reference to condensation: a review, Int. J. Multiphase Flow 845–859 (2011).
[50] J.A. Albers, R.P. Macosko, Experimental pressure-drop investigation of nonwetting, condensing flow of mercury vapor in a constant-diameter tube in 1-g and zero-gravity environments, NASA TN D-2838 (1965) 1–32.
[51] J.A. Albers, R.P. Macosko, condensation pressure drop of nonwetting mercury in a uniformly tapered tube in 1-g and zero-gravity environments, NASA TN D-3185 (1966) 1–38.
[52] D. Namkoong, H.B. Block, R.P. Macosko, C.C. Crabs, Photographic study of condensing mercury flow in 0- and 1-g environments, NASA TN D-4023 (1967) 1–31.
[53] E.G. Keshock, Experimental and analytical investigation of 0-g condensation in a mechanical refrigeration system application, TR 75-T6, Old Dominion University, Contract NAS9-13410 (1975) 1–92.
[54] H. Lee, I. Mudawar, M.M. Hasan, Experimental and theoretical investigation of annular flow condensation in microgravity, Int. J. Heat Mass Transfer 61 (2013) 293–309.
[55] H. Lee, I. Park, C. Konishi, I. Mudawar, R.I. May, J.R. Juergens, J.D. Wagner, N.R. Hall, H.K. Nahra, M.M. Hasan, J.R. Mackey, Experimental investigation of flow condensation in microgravity, J. Heat Transfer 136 (2014) 021502-1–11.
[56] B.-X. Wang, X.-Z. Du, Study on laminar film-wise condensation for vapor flow in an inclined small/mini-diameter tube, Int. J. Heat Mass Transfer 43 (2003) 1859–1868.
[57] S. Lips, J.P. Meyer, Experimental study of convective condensation in an inclined smooth tube. Part I: inclination effect on flow pattern and heat transfer coefficient, Int. J. Heat Mass Transfer 55 (2012) 395–404.
[58] S. Lips, J.P. Meyer, Experimental study of convective condensation in an inclined smooth tube. Part II: inclination effect on pressure drops and void fractions, Int. J. Heat Mass Transfer 55 (2012) 405–412.
[59] J. Kurita, M. Kivisalu, S. Mitra, R. Naik, A. Narain, Experimental results on gravity driven fully condensing flows in vertical tubes, their agreement with theory, and their differences with shear driven flows' boundary-condition sensitivities, Int. J. Heat Mass Transfer 54 (2011) 2932–2951.
[60] S. Mitra, A. Narain, R. Naik, S.D. Kulkarni, A quasi one-dimensional method and results for steady annular/stratified shear and gravity driven condensing flows, Int. J. Heat Mass Transfer 54 (2011) 3761–3776.
[61] I. Park, L.E. O'Neill, C.R. Kharangate, I. Mudawar, Assessment of body force effects in flow condensation, Part I: experimental investigation of liquid film behavior for different orientations, Int. J. Heat Mass Transfer 106 (2017) 295–312.
[62] L.E. O'Neill, I. Park, C.R. Kharangate, V.S. Devahdhanush, V. Ganesan, I. Mudawar, Assessment of body force effects in flow condensation, part II: criteria for negating influence of gravity, Int. J. Heat Mass Transfer 106 (2017) 313–328.
[63] S.M.A. Noori Rahim Abadi, J.P. Meyer, J. Dirker, Effect of inclination angle on the condensation of R134a inside an inclined smooth tube, Chem. Eng. Res. Des. 132 (2018) 346–357.
[64] I. Mudawar, Flow boiling and flow condensation in reduced gravity, Adv. Heat Transfer 49 (2017) 225–306.
[65] H. Zhang, I. Mudawar, M.M. Hasan, Experimental assessment of the effects of body force, surface tension force, and inertia on flow boiling CHF, Int. J. Heat Mass Transfer 45 (2002) 4079–4095.
[66] H. Zhang, I. Mudawar, M.M. Hasan, Flow boiling CHF in microgravity, Int. J. Heat Mass Transfer 48 (2005) 3107–3118.
[67] C. Konishi, I. Mudawar, Review of flow boiling and critical heat flux in microgravity, Int. J. Heat Mass Transfer 80 (2015) 469–493.
[68] H. Lee, C.R. Kharangate, N. Mascarenhas, I. Park, I. Mudawar, Experimental and computational investigation of vertical downflow condensation, Int. J. Heat Mass Transfer 85 (2015) 865–879.
[69] C.R. Kharangate, H. Lee, I. Park, I. Mudawar, Experimental and computational investigation of vertical upflow condensation in a circular tube, Int. J. Heat Mass Transfer 95 (2016) 249–263.
[70] C.R. Kharangate, I. Mudawar, Review of computational studies on boiling and condensation, Int. J. Heat Mass Transfer 108 (2017) 1164–1196.
[71] L.E. O'Neill, I. Mudawar, M.M. Hasan, H.K. Nahra, R. Balasubramaniam, J.R. Mackey, Flow condensation pressure oscillations at different orientations, Int. J. Heat Mass Transfer 127 (2018) 784–809.
[72] S.M. Kim, I. Mudawar, Universal approach to predicting two-phase frictional pressure drop for adiabatic and condensing mini/micro-channel flows, Int. J. Heat Mass Transfer 55 (2012) 3246–3261.
[73] S.M. Kim, I. Mudawar, Universal approach to predicting heat transfer coefficient for condensing mini/micro-channel flow, Int. J. Heat Mass Transfer 56 (2013) 238–250.
[74] L.E. O'Neill, R. Balasubramaniam, H.K. Nahra, M.M. Hasan, J.R. Mackey, I. Mudawar, Identification of condensation flow regime at different orientations using temperature and pressure measurements, Int. J. Heat Mass Transfer 135 (2019) 569–590.
[75] L.E. O'Neill, C.R. Kharangate, I. Mudawar, Time-averaged and transient pressure drop for flow boiling with saturated inlet conditions, Int. J. Heat Mass Transfer 103 (2016) 133–153.
[76] L.E. O'Neill, I. Mudawar, M.M. Hasan, H.K. Nahra, B. Ramaswamy, N.R. Hall, A. Lokey, J.R. Mackey, Experimental investigation into the impact of density wave oscillations on flow boiling system dynamic behavior and stability, Int. J. Heat Mass Transfer 120 (2018) 144–166.
[77] L.E. O'Neill, I. Mudawar, Mechanistic model to predict frequency and amplitude of density wave oscillations in vertical upflow boiling, Int. J. Heat Mass Transfer 123 (2018) 143–171.
[78] L.E. O'Neill, I. Mudawar, M.M. Hasan, H.K. Nahra, B. Ramaswamy, J.R. Mackey, Experimental investigation of frequency and amplitude of Density Wave Oscillations in vertical upflow boiling, Int. J. Heat Mass Transfer 125 (2018) 1240–1263.
[79] J. Chen, W. Li, Local convective condensation heat transfer in horizontal double-layer three-dimensional dimple-grooved tubes, Int. J. Heat Mass Transfer 127 (2018) 810–820.
[80] J.R. Thome, J. El Hajal, A. Cavallini, Condensation in horizontal tubes, part 2: new heat transfer model based on flow regimes, Int. J. Heat Mass Transfer 46 (2003) 3365–3387.
[81] J.P. Meyer, D.R.E. Ewim, Heat transfer coefficients during the condensation of low mass fluxes in smooth horizontal tubes, Int. J. Multiphase Flow 99 (2018) 485–499.
[82] Y. Camaraza-Medina, A. Hernandez-Guerrero, J.L. Luviano-Ortiz, K. Mortensen-Carlson, O.M. Cruz-Fonticiella, O.F. Garcia-Morales, New model for heat transfer calculation during film condensation inside pipes, Int. J. Heat Mass Transfer 128 (2019) 344–353.
[83] R.K. Shah, A.L. London, Laminar Flow Forced Convection in Ducts: A Source Book for Compact Heat Exchanger Analytical Data, Academic Press, New York, 1978.
[84] S.M. Kim, I. Mudawar, Theoretical model for annular flow condensation in rectangular micro-channels, Int. J. Heat Mass Transfer 55 (2012) 958–970.
[85] G.B. Wallis, One-Dimensional Two-Phase Flow, McGraw-Hill, New York, 1969.
[86] I. Mudawar, M.A. El-Masri, Momentum and heat transfer across freely-falling turbulent liquid films, Int. J. Multiphase Flow 12 (1986) 771–790.
[87] S.-M. Kim, I. Mudawar, Review of databases and predictive methods for heat transfer in condensing and boiling mini/micro-channel flows, Int. J. Heat Mass Transfer 77 (2014) 627–652.
[88] W.W. Akers, H.F. Rosson, Condensation inside a horizontal tube, Chem. Eng. Prog. Symp. 56 (1960) 145–149.
[89] A. Cavallini, R. Zecchin, A dimensionless correlation for heat transfer in forced convection condensation, in: Proc. Fifth Int. Heat Transfer Conf., Tokyo, Japan, vol. 3, 1974, pp. 309–313.
[90] M.M. Shah, A general correlation for heat transfer during film condensation inside pipes, Int. J. Heat Mass Transfer 22 (1979) 547–556.
[91] H. Haraguchi, S. Koyama, T. Fujii, Condensation of refrigerants HCFC 22, HFC 134a and HCFC 123 in a horizontal smooth tube (2nd report), Trans. JSME (B) 60 (1994) 245–252.

[92] K.W. Moser, R.L. Webb, B. Na, A new equivalent Reynolds number model for condensation in smooth tubes, J. Heat Transfer 120 (1998) 410–417.
[93] L. Friedel, Improved friction pressure drop correlations for horizontal and vertical two phase pipe flow, Paper E2, in: European Two Phase Flow Group Meeting, Ispra, Italy, 1979.
[94] M.M. Shah, An improved and extended general correlation for heat transfer during condensation in plain tubes, HVAC&R Res. 15 (5) (2009) 889–913.
[95] W.W. Wang, T.D. Radcliff, R.N. Christensen, A condensation heat transfer correlation for millimeter-scale tubing with flow regime transition, Exp. Therm. Fluid Sci. 26 (2002) 473–485.
[96] S. Koyama, K. Kuwahara, K. Nakashita, K. Yamamoto, An experimental study on condensation of refrigerant R134a in a multi-port extruded tube, Int. J. Refrig. 24 (2003) 425–432.
[97] X. Huang, G. Ding, H. Hu, Y. Zhu, H. Peng, Y. Gao, B. Deng, Influence of oil on flow condensation heat transfer of R410A inside 4.18 mm and 1.6 mm inner diameter horizontal smooth tubes, Int. J. Refrig. 33 (2010) 158–169.
[98] T. Bohdal, H. Charun, M. Sikora, Comparative investigations of the condensation of R134a and R404A refrigerants in pipe minichannels, Int. J. Heat Mass Transfer 54 (2011) 1963–1974.
[99] J.E. Park, F. Vakili-Farahani, L. Consolini, J.R. Thome, Experimental study on condensation heat transfer in vertical minichannels for new refrigerant R1234ze€ versus R134a and R236fa, Exp. Therm. Fluid Sci. 35 (2011) 442–454.